Agricultural and Forest Meteorology 310 (2021) 108484

Contents lists available at ScienceDirect

Agricultural and Forest Meteorology

journal homepage: www.elsevier.com/locate/agrformet

Measuring surface temperatures in a woodland savanna: Opportunities and challenges of thermal imaging in an open-canopy ecosystem

Miriam R. Johnston [a,*], Ana Andreu [b,c], Joseph Verfaillie [b], Dennis Baldocchi [b], María P. González-Dugo [c], Paul R. Moorcroft [a]

[a] Dept. of Organismic and Evolutionary Biology, Harvard University, 26 Oxford St, Cambridge, MA 02138, USA
[b] Dept. of Environmental Science, Policy and Management, University of California, Berkeley, 130 Hilgard Way, Berkeley, CA 94720, USA
[c] IFAPA, Consejeria de Agricultura, Pesca y Desarrollo Rural, Apdo. 3048 ES-14071, Cordoba, Spain

ARTICLE INFO

Keywords:
Plant temperature
Thermal camera
Woodland savanna
Emissivity
Two-source energy balance model

ABSTRACT

In open-canopy ecosystems, thermal imaging affords an unprecedented opportunity to resolve concurrent temperatures of overstory vegetation, understory vegetation, and soil across space and time. This simultaneous view of ecosystem components promises a holistic understanding of ecosystem energy status, defines diverse thermal niches, and can provide a full suite of thermal measurements to drive ecosystem energy budget models. However, thermal imaging in open-canopy ecosystems also presents challenges: emissivity and background radiation data required for image calibration are variable across the scene; mixed pixels can be misleading because of divergent component temperatures; and targets of interest have very different pixel dimensions associated with their different distances from the camera. In this study, we evaluated effects of these challenges on calculated target temperatures, and we contextualized those results with five months of half-hourly thermal images, over vs. understory radiation measurements, ground-based emissivity estimates, and an application of thermal images to drive the two-source energy balance model (TSEB) in a Californian woodland savanna. We found that, though background radiation conditions varied considerably at different locations within the ecosystem, the high emissivities of the ecosystem components minimized the effect of that variation on calibrated target temperatures. Different pixel dimensions (i.e. variable geographical space covered by a single thermal image pixel) were associated with changes of temperature minima and maxima by over one degree Celsius, but they had little effect on aggregate summary values (e.g. estimates of mean temperature). Conversely, mixed pixels, given the relatively widely divergent component temperatures in our heterogeneous system, had the potential to influence calibrated target temperatures dramatically, by several degrees Celsius. The TSEB results corroborate these findings: they are sensitive to differences in component temperatures, while emissivity and reflected radiation corrections result in a negligible difference in sensible heat flux predictions.

1. Introduction

Plant temperature exerts fundamental control on physiological processes such as photosynthesis (Farquhar et al., 1980; Way and Yamori, 2014), respiration (Heskel et al., 2016), transpiration (Gates, 1968), and growth and development (Michaletz, 2018). It has long been recognized as an indicator of plant water relations (Brown and Escombe, 1905), and has been used to assess moisture stress at scales from individuals (Jackson et al., 1977) to continents (Anderson et al., 2007). At an ecosystem-scale, plant and soil temperatures influence fluxes of carbon, water, and energy and play a key role in energy budget closure (Heusinkveld et al., 2004; Meyers and Hollinger, 2004).

Ecosystem structure can strongly influence vegetation thermal environments and therefore productivity (Rotenberg and Yakir, 2010). Open-canopy, semi-arid and Mediterranean ecosystems are subject to seasonal water deficit, fire, grazing pressure, and high incoming radiation, yet they are typically carbon sinks, even during extended drought (Ma et al., 2016; Rotenberg and Yakir, 2010). Structure (in addition to phenology [Maseyk et al., 2008], plant physiology [Baldocchi et al., 2004], and rooting depth [Miller et al., 2010]) appears to play an important role in a savanna's ability to maintain function: the low density of trees results in high aerodynamic roughness and strong canopy-atmosphere coupling, which makes the system an efficient convector of sensible heat. Therefore, despite the high radiation loading,

* Corresponding author.
E-mail address: johnston.miriam@gmail.com (M.R. Johnston).

https://doi.org/10.1016/j.agrformet.2021.108484
Received 14 August 2020; Received in revised form 16 March 2021; Accepted 14 May 2021
Available online 6 September 2021

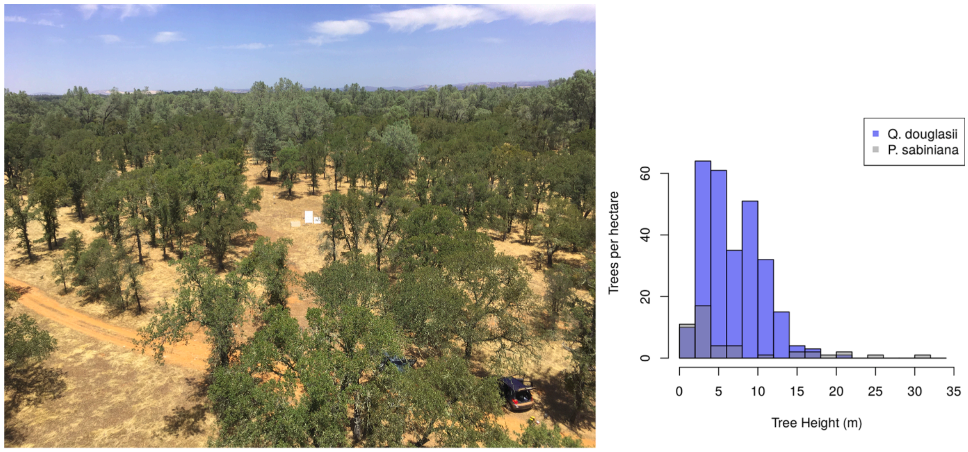

(a) (b)

Fig. 1. (a) View of field site looking northeast from the main fluxtower. Foreground trees are *Q. douglasii* and taller background trees are *P. sabiniana*. Solar panels and concrete reference panel are visible in the center of the image, and there is a road in the lower left corner. (b) *Q. douglasii* and *P. sabiniana* heights and density, based on a census of fourteen circular plots totaling 9610 m^2; only trees >1.59 m tall were counted. (The reader is referred to the web version of this article for colors.)

low albedo (compared to shrublands and grasslands), and seasonally very low precipitation, savannas can maintain a relatively low canopy surface temperature and physiologically favorable carbon, water, and energy balances (Baldocchi et al., 2004; Rotenberg and Yakir, 2010). In this context, long-term and spatially resolved temperatures of the various components of a savanna system (e.g. soil, understory grass, and overstory trees) are of great interest.

Field-deployable thermal cameras are a promising tool with which to measure these temperatures (Aubrecht et al., 2016; Kim et al., 2016, 2018; Pau et al., 2018; Still et al., 2019). Aubrecht et al. (2016) provide an excellent summary of thermal camera calibration theory, a sensitivity analysis for calibration parameters, and a camera sensor noise and accuracy assessment. They also demonstrate the utility of thermal cameras to measure canopy temperature in an eastern deciduous forest and an evergreen needleleaf forest (Aubrecht et al., 2016). Here, we extend Aubrecht et al.'s thermal imaging guide to the case of heterogeneous, open-canopy ecosystems. While thermal imaging of an open-canopy ecosystem presents an opportunity to measure vertically and horizontally disparate components of the system concurrently, it may also introduce challenges which are (comparatively) absent when imaging a closed canopy. Specifically, background radiation conditions (i.e. radiation from the surroundings that reflects off the target of interest) vary significantly for regions of interest at different vertical heights, emissivity is variable across ecosystem components, thermal image pixels correspond to variable geographical space associated with the varying distances of targets from the camera, and ecosystem heterogeneity amplifies the confounding effects of mixed pixels.

In this paper, we: (1) quantify the theoretical effects of the potential challenges associated with thermal imaging in open-canopy systems; (2) assess the functional importance of these challenges in a Californian blue oak (*Quercus douglasii*) woodland savanna; and (3) contextualize the calibration challenges and demonstrate an opportunity offered by thermal imaging in an open-canopy system by using thermal images to generate sensible heat flux estimations, including geographical heterogeneity, with the two-source energy balance model (TSEB, Norman et al., 1995). Additionally, we include an analysis of the effect of the thermal camera's protective enclosure on calibrated temperatures.

2. Materials and methods

2.1. Site description

The camera deployment site is a seasonally-grazed oak savanna at 177 m of elevation in the lower foothills of California's Sierra Nevada Mountains (38.438N, 120.968W). The overstory is open (leaf area index approximately 0.7, with considerable variation) and comprised mainly of deciduous *Quercus douglasii* ("oak") interspersed with less numerous but considerably taller *Pinus sabiniana* ("pine", Baldocchi et al., 2010, Fig. 1). The understory is dominated by annual C3 grass species, mostly *Brachypodium, Hypochaeris*, and *Bromus*. Three phenological strategies are evident at this site: the oaks flush their leaves in early spring and drop them in the autumn; the understory is green during spring, senesces in the dry season (June - October), and has a variable second green-ness peak during the winter; and the pines keep needles for several years.

The soil is a silt loam to rocky silt loam, approximately 1 m deep and underlain by saprolite and fractured metamorphic and sedimentary rock (Miller et al., 2010). Depth to the water table varies geographically and seasonally, but is typically 7–12 m, and the oaks are considered obligate phreatophytes (Miller et al., 2010).

The climate is Mediterranean; summers are hot and dry, while winters are mild and wet. Mean annual air temperature is 15.8 °C, and most years the minimum temperature dips below freezing and the maximum exceeds 40 °C. Mean annual precipitation is 559 mm and usually falls only November - May. Annual net shortwave radiation is typically about 200 W/m^2, and annual net longwave radiation is around -85 W/m^2. For each of 15 years of eddy covariance measurements (2001-15, Ameriflux code US-Ton), this woodland savanna has been a carbon sink, with an overall mean net ecosystem exchange of 110 g C m^{-2} year^{-1} (standard deviation: 57 g C m^{-2} year^{-1}, Ma et al., 2016).

The site is extensively instrumented (Fig. 2). For the thermal camera data calibrations, we used half-hourly data from two net radiometers and an air temperature/relative humidity probe (see Appendix A for thermal camera calibration instrumentation details). We compared camera measurements to infrared thermometer (IRT) measurements (Apogee Instruments SI-121, Logan, UT, USA; measurement uncertainty of ±0.2 °C when detector and target are within 20 °C) and thermocouple (TC) measurements of a WonderBoard Lite concrete panel near the center of the camera's field of view (Fig. 1a). For the TSEB analysis, in addition to the probe and radiometer data, we inputted wind speed as measured by a 3D sonic anemometer (WindMaster 1590, Gill Instruments Ltd., Lymington, UK) and soil heat flux measured by heat flux plates (Hukseflux, model HFP01, Delft, The Netherlands). We compared TSEB's predictions to sensible heat fluxes calculated as part of a Li-Cor LI-7500A (Lincoln, NE, USA) eddy covariance system (Baldocchi et al., 2004; Ma et al., 2007; Xu and Baldocchi, 2004). The overstory instrumentation is mounted at about 21 m above ground level, and the

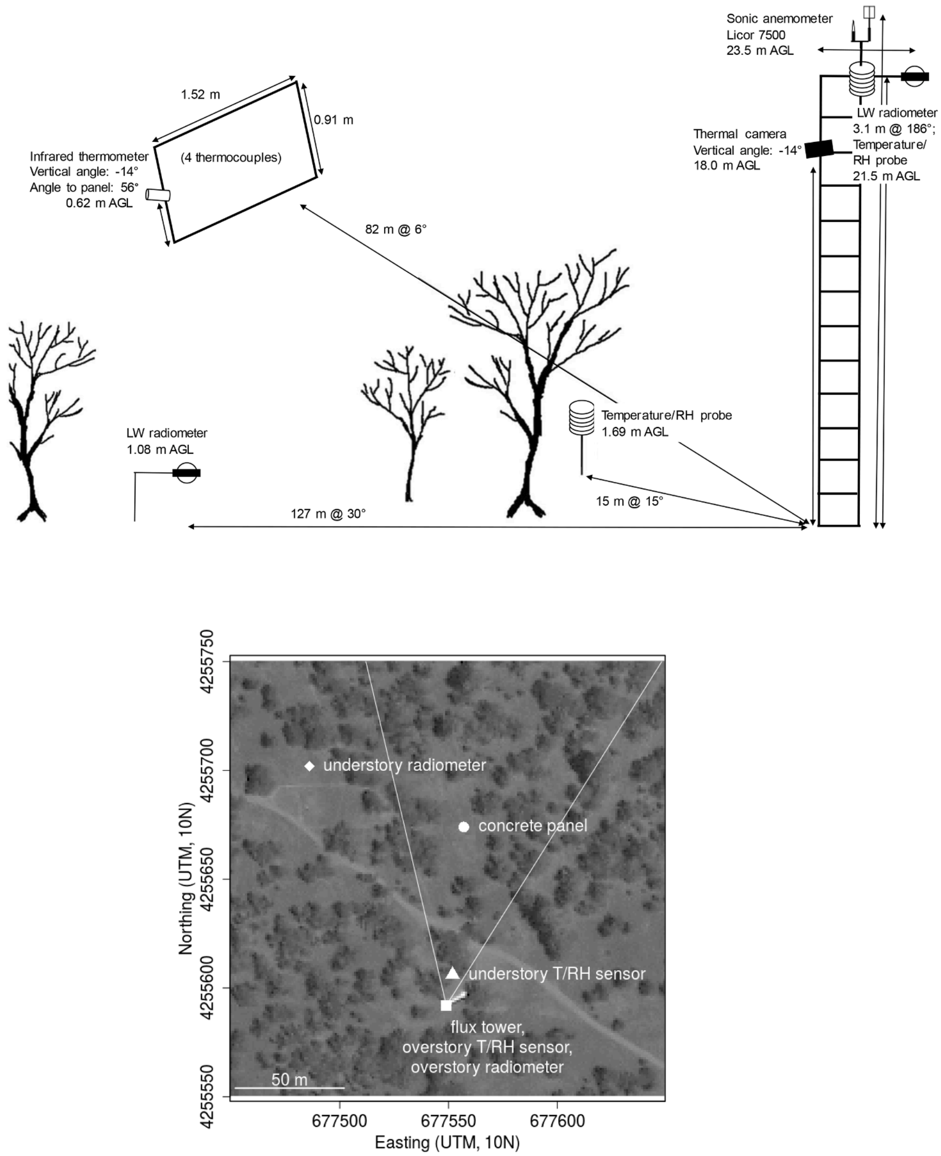

(a)

(b)

Fig. 2. (a) Schematic and (b) aerial image of the site setup and instrument locations. White lines show the approximate FLIR angle and direction of view. Radiometer fields of view are approximately hemispherical (180°); infrared thermometer footprint on the concrete panel is about 0.4 m^2. “AGL” is “above ground level;” “RH” is “relative humidity;” “LW” is “longwave”.

understory at about 1 m (Fig. 2).

2.2. Thermal camera deployment

We deployed a FLIRA325sc thermal camera on the northeast corner of the main flux tower, 18.4 m high, pointed about 14 degrees down from the horizontal, and largely shaded by the rest of the tower at midday. It was enclosed in aluminum housing fitted with a sun shield and an anti-reflection-coated germanium window (50 mm diameter, 3 mm thick, 8–12 μm anti-reflection-coated). The camera has a resolution of 320 x 240 pixels, and its field of view captured patches of open grass, bare soil, and oak and pine individuals (Fig. 1a). The company-reported accuracy is ±2°C or ±2% of the reading; the standard temperature range is -20 - 120 °C. For FLIR data collection technical details, please see Appendix B.

Between June 1, 2019 and October 31, 2019, we collected 7340 thermal images, one at each half hour (i.e. 48 measurements per 24 h period) except for four (2019-07-02 18:30, 2019-07-03 13:30, 2019-07-03 14:00, and 2019-10-24 11:00 PST), for which our automatic saving protocol failed (see Appendix B). We omitted an additional 19 photos from analysis due to the confounding effects of precipitation, during which it is impossible to distinguish vegetation temperature from the temperature of the water in the air (Aubrecht et al., 2016). We also omitted 120 photos due to missing micrometeorological data required for calibration. In sum, we analyzed 7224 photos over the five-month period. During this time, the grass was senescent and the oaks had leaves. We analyzed several regions of interest (ROIs) for each ecosystem component (Fig. 3).

We mounted the concrete WonderBoard Lite concrete reference panel on the ground, 84.5 m from the camera (Figs. 1a, 2, 3). The TCs were nestled into holes and secured with concrete putty, and the IRT was aimed at the panel’s center. While using a distant, thermally non-conductive reference panel likely yielded poorer camera/reference comparisons than a metal panel mounted closer to the camera, it gave a more realistic idea of the accuracy with which the camera can measure distant soil and vegetation.

2.3. Image calibration with the enclosure window

We refer the reader to Aubrecht et al. (2016) for a detailed background on thermal imaging in the field, to Still et al. (2019) for an overview of thermal camera ecological applications, and to Appendix A for a summary of calibration terms and equations. Here, we extend Aubrecht et al.'s calibration analysis to the case in which the camera is in a protective enclosure. Since the window of the enclosure is not perfectly transmissive and has a certain degree of reflectivity, it will influence the energy measured by the camera, both by attenuating the signals from the target, surroundings, and air, and by contributing its own energy.

Ideally, a thermal camera would measure the internal energy of its target, which is directly related to the target's temperature. In reality, the camera measures thermal energy from the target, from the surroundings/background reflecting off the target, and from other entities in the imaging path, such as the air. The thermal energies (Φ, Eqn. 1) of everything the camera measures are mediated by: (i) the emissivity of the radiating object and (ii) the transmissivities of the media through which energy moves on its way to the sensor (Fig. 4).

The total energy received by the camera's sensor is described by (Eqn. 1):

$$\underbrace{\Phi_{total}}_{\text{energy at sensor}} = \underbrace{\Phi_{target}\epsilon_{target}\tau_{air}\tau_{win}}_{\text{target energy is mediated by } \epsilon_{target} \text{ and all } \tau} + \underbrace{\Phi_{refl}\epsilon_{refl}\left(1-\epsilon_{target}\right)\tau_{air}\tau_{win}}_{\text{reflected energy off target; } \tau_{target}=0, \text{ so } R_{target} = 1-\epsilon_{target}} + \underbrace{\Phi_{air}\left(1-\tau_{air}\right)\tau_{win}}_{\text{energy of air between target and window; } \epsilon_{air}=1-\tau_{air}} + \underbrace{\Phi_{win}\left(1-R_{win}-\tau_{win}\right)}_{\text{energy of window mediated by } \epsilon_{win} = 1- R_{win} - \tau_{win}}, \tag{1}$$

where Φ is thermal energy in camera-specific units (Appendix A), ϵ is emissivity, τ is transmissivity, R is reflectivity, and the subscripts denote the target ("target"), surrounding entities ("refl"), air between the sensor and the target ("air"), and enclosure window ("win"). Solve for Φ_{target} (Eqn. 2) and apply a modified Planck equation (Eqn. 3) to convert to temperature (Aubrecht et al., 2016):

$$\Phi_{target} = \frac{\Phi_{total}}{\epsilon_{target}\tau_{air}\tau_{win}} - \frac{\Phi_{refl}\epsilon_{refl}\left(1-\epsilon_{target}\right)}{\epsilon_{target}} - \frac{\Phi_{air}\left(1-\tau_{air}\right)}{\epsilon_{target}\tau_{air}} - \frac{\Phi_{win}\left(1-R_{win}-\tau_{win}\right)}{\epsilon_{target}\tau_{air}\tau_{win}} \tag{2}$$

$$T = \frac{B}{ln\left(\frac{R_1}{R_2(\Phi+O)}+F\right)}, \tag{3}$$

where T is temperature and B, $R1$, $R2$, O, and F are Planck function coefficients reported in the FLIR image header. Because of the nonlinear relationship between temperature and energy, we made calculations with surface temperature (e.g. computing mean temperatures of ROIs) by applying the inverse of (Eqn. 3), making the calculations with Φ, and then re-converting to temperature.

The assumptions embedded in (Eqns. 1 and 2) are that the air is unreflective ($R_{air} = 0$), the target is non-transmissive ($\tau_{target} = 0$), and there are no higher-than-first order reflections of thermal energy (though higher-order reflections may effectively be included in calculation of Φ_{refl}). Additionally, we omitted a term for energy reflected off the face of the window on the inside of the enclosure because the plastic ring surrounding the camera's lens touches the window, effectively minimizing this contribution. We also omitted terms describing the energy and transmissivity of the air between the window and the sensor because this air mass is small enough to have negligible influence on

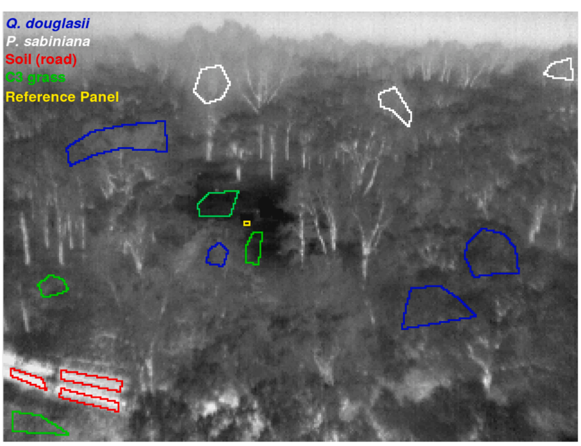

Fig. 3. We selected regions of interest which had a relatively small area, so that the entire ROI was a similar distance away from the camera (Aubrecht et al., 2016). We left a buffer of one pixel (for the concrete panel) to several pixels (for other targets, as defined by eye) around each ROI so that results would be undisturbed by slight field of view shifts. Required buffer size is contingent on stability of the camera mount, wind, and target response to wind. (The reader is referred to the web version of this article for colors.)

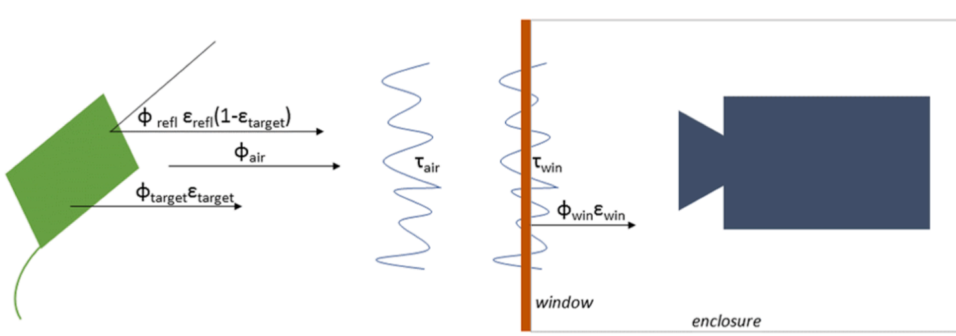

Fig. 4. Schematic of the camera set-up in the field. The camera receives thermal energy from the target (Φ_{target}), surrounding entities whose radiation reflects off the target (Φ_{refl}), the air between its sensor and the target (Φ_{air}), and the window of its enclosure (Φ_{window}). Those energies are mediated by the emissivity of the target (ϵ_{target}), the emissivity of the reflecting objects (ϵ_{refl}), the emissivity of the window (ϵ_{win}), and the transmissivites of both the air and the window (τ_{air} and τ_{win}).

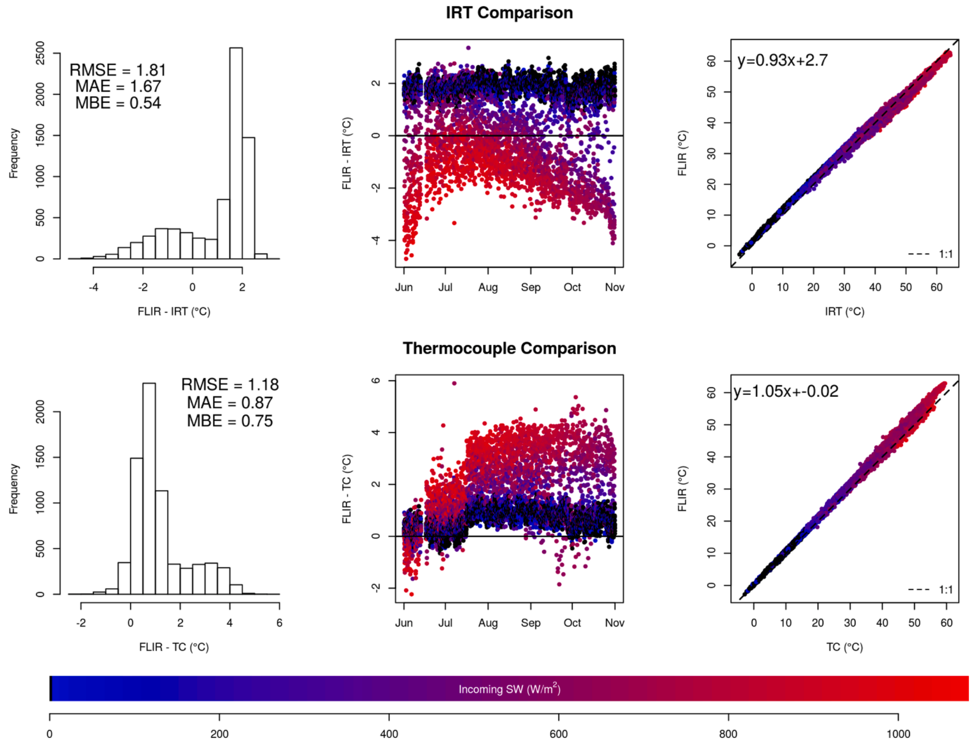

Fig. 5. Summary of the comparison between the IRT/mean TC and the calibrated FLIR measurement. Colors are scaled according to incoming shortwave radiation; black is incoming SW = 0 W/m^2, blue is lower radiation, and red is higher. (For interpretation of the references to color in this figure legend, the reader is referred to the web version of this article.)

Table 1
TSEB configurations. T_C is canopy temperature, T_S is substrate temperature, and T_R is bulk radiometric surface temperature (Eqn. D.1). For configurations 1–4, temperatures are mean pixel temperatures of the components indicated, where pixels have been aggregated to a common size (31.6 cm) and are weighted equally, regardless of ROI. In configurations 1, 2, 3, and 5, the proportion of oak and pine comprising T_C is based on the fractional cover of these components within the tower footprint, calculated using a sharpened and classified IKONOS image.

Configuration	T_C component	T_S component	Emissivity, reflected radiation
1	Weighted average of oak (94%) and pine	Dry grass	$\epsilon = 0.95$; $\Phi_{refl} = \Phi_{sky}$
2	Weighted average of oak (94%) and pine	Dry grass	ϵ, Φ_{refl} as measured
3	Weighted average of oak (94%) and pine	Soil	ϵ, Φ_{refl} as measured
4	T_R derived from T_C and T_S of Run 3 via Eqn. D.1		ϵ, Φ_{refl} as measured
5*	Randomly selected single pixel from T_C pool	Randomly selected single pixel from T_S (grass) pool	ϵ, Φ_{refl} as measured
*One hundred repetitions			

calibrated temperatures.

We calculated the germanium window's transmissivity and reflectivity by averaging the convolution of the company's transmissivity and reflectivity curves with the camera's spectral response, 7.5 - 13 μm (Fig. A.1). To quantify the energy of the window itself (Φ_{win}), we measured window temperature with a thermocouple affixed to it, inside the enclosure and out of the camera's view. We quantified the effect of including the enclosure window in calibrations by comparing calibrated FLIR-measured temperatures of the concrete panel given measured window parameters vs. assuming that $\tau_{win} = 1$ and $R_{win} = 0$.

2.4. Challenges of thermal imaging in an open-canopy system

2.4.1. Background radiation and emissivity

Background longwave radiation is used to define "reflected radiation," which originates from non-target entities (e.g. the sky, surrounding vegetation, eddy covariance tower infrastructure, etc.), reflects off the target of interest, and contributes to the apparent radiance from that target. Because a thermal camera can not distinguish between the radiation emitted by a target as a function of its temperature and the radiation reflected by that target, it is necessary to correct thermal images for reflected energy. The proportion of reflected radiation vs. emitted radiation as measured by a thermal camera is

Table 2
Summary metrics for the differences between FLIR and mean thermocouple measurements and between FLIR and IRT measurements of the concrete panel ($n_{all} = 7059$ comparisons, $n_{day} = 3903$, $n_{night} = 3156$). *RMSE* is the root mean squared error, *MAE* is the mean absolute error, *MBE* is the mean bias error, *Q1* is the first quartile of the difference, *Med* is the median, *Q3* is the third quartile, and *SD* is the standard deviation. Day was defined as times when incoming SW radiation was >0 W/m^2. All units are °C.

Comparison	RMSE	MAE	MBE	Q1	Med	Q3	SD
FLIR - TC_{mean}, all	1.59	1.19	1.15	0.47	0.84	1.42	1.10
FLIR - TC_{mean}, day	2.03	1.62	1.56	0.58	1.19	2.63	1.29
FLIR - TC_{mean}, night	0.75	0.66	0.65	0.37	0.68	0.94	0.39
FLIR - IRT, all	1.75	1.63	0.94	0.03	1.64	1.96	1.48
FLIR - IRT, day	1.63	1.46	0.21	-1.13	0.36	1.74	1.64
FLIR - IRT, night	1.88	1.85	1.85	1.65	1.87	2.06	0.30

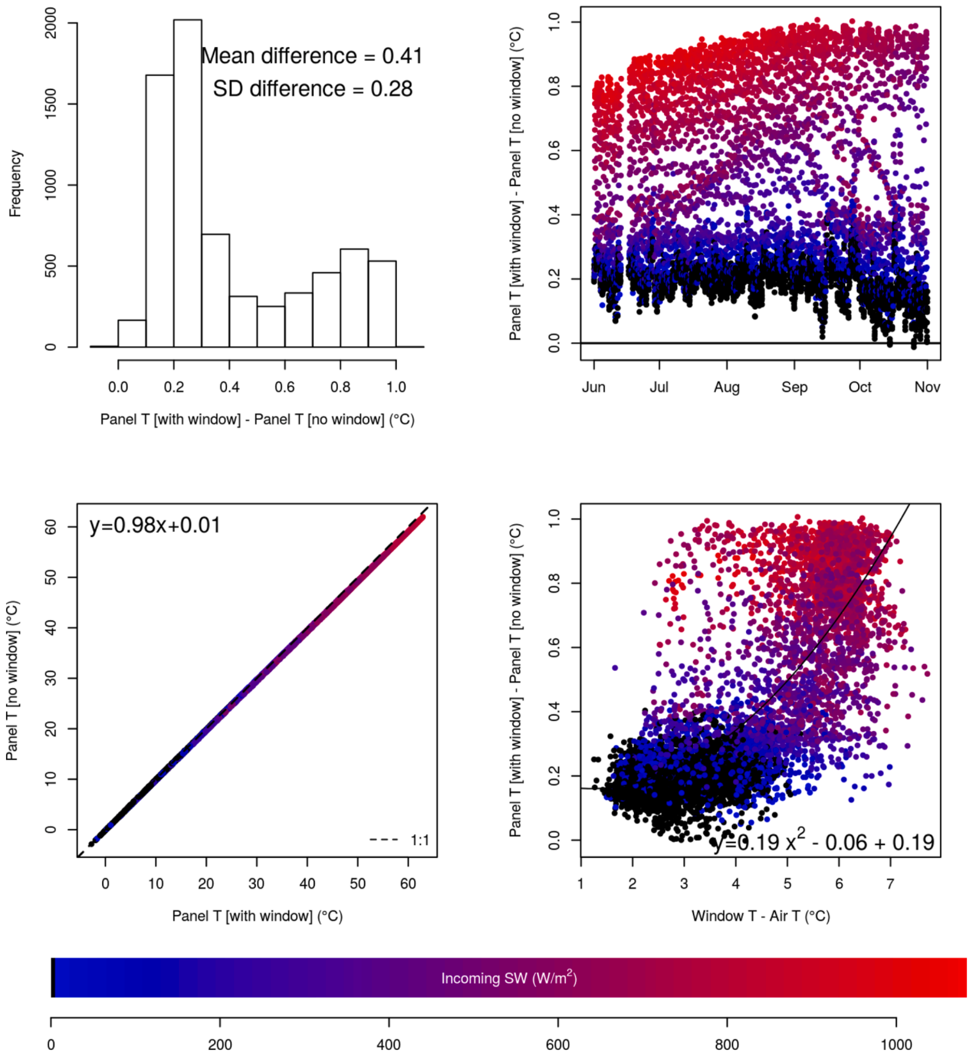

Fig. 6. Summary of the comparison between FLIR measurements of the concrete reference panel when the window is taken into account in the calibrations "[with window]" vs. when it is omitted "[no window]". Colors are scaled according to incoming shortwave radiation; black is incoming SW = 0 W/m^2, blue is lower radiation, and red is higher. (For interpretation of the references to color in this figure legend, the reader is referred to the web version of this article.)

defined by the target's emissivity. If the target were a perfect black body (emissivity = 1), it would absorb and re-radiate all radiation incident upon it and thus there would be no reflected radiation. Conversely, in the case where the target's emissivity is less than 1, the apparent radiative signal from the target is a combination of the radiance emitted by the target and the radiance it reflects (Eqn. 4):

$$E_{apparent} = \left[\epsilon_{target} * E_{target}\right] + \left[\left(1 - \epsilon_{target}\right) * E_{reflected}\right], \tag{4}$$

where $E_{apparent}$ is the apparent energy from the target (measured by the sensor), E_{target} is the energy emitted by the target according to its temperature, $E_{reflected}$ is reflected energy, and ϵ_{target} is the target's emissivity.

When a thermal camera is mounted above a closed canopy, most reflected radiation originates from the sky (e.g. Aubrecht et al., 2016). Additionally, in a closed-canopy ecosystem in which all targets are green vegetation, it may be comparatively more justifiable to assume that all targets have the same emissivity (e.g. Aubrecht et al., 2016; Kim et al., 2016, 2018; Pau et al., 2018; though no one, to our knowledge, has rigorously tested this assumption). However, in an open-canopy ecosystem, targets of interest plausibly reflect radiation both from the sky and from the surrounding vegetation, and heterogeneous, phenologically-diverse ecosystem components (soil, grass, oaks, and pines) may require a more nuanced treatment of emissivities.

We quantified background reflected radiation separately for the oaks/pines and the grass/soil, obtaining Φ_{refl} in camera units by estimating it from temperature of the reflecting objects using the inversion of (Eqn. 3). For the trees, we assumed that reflected radiation was coming from all directions – from the sky, the other trees, and the ground. The balance of those contributors was unknown and variable by ROI; for simplicity, we assumed that half of the reflected radiation was from below and half from the same level/above. We assumed that radiation reflecting off the grass and the soil was from above (from both sky and trees).

As was the case for the camera measurements, obtaining accurate reflecting object temperatures from radiometer measurements required background radiation and emissivity estimates. We calculated the temperature of the tree/sky reflecting entities from understory measurements of incoming LW radiation, mediated by emissivity according to (Eqn. 5) and reflecting understory-measured outgoing LW (Fig. 2, Appendix A). We calculated the temperature of the ground reflecting entities from the understory outgoing LW measurement, mediated by grass emissivity and reflecting incoming LW. Total emissivity of the surroundings contributing reflected energy to trees was quantified by (Eqn. 6).

$$\epsilon_{reflected,soilandgrass} = \left(f_{pine} * \epsilon_{pine}\right) + \left(f_{oak} * \epsilon_{oak}\right) + \left[\left(1 - f_{pine} - f_{oak}\right) * \epsilon_{sky}\right], \tag{5}$$

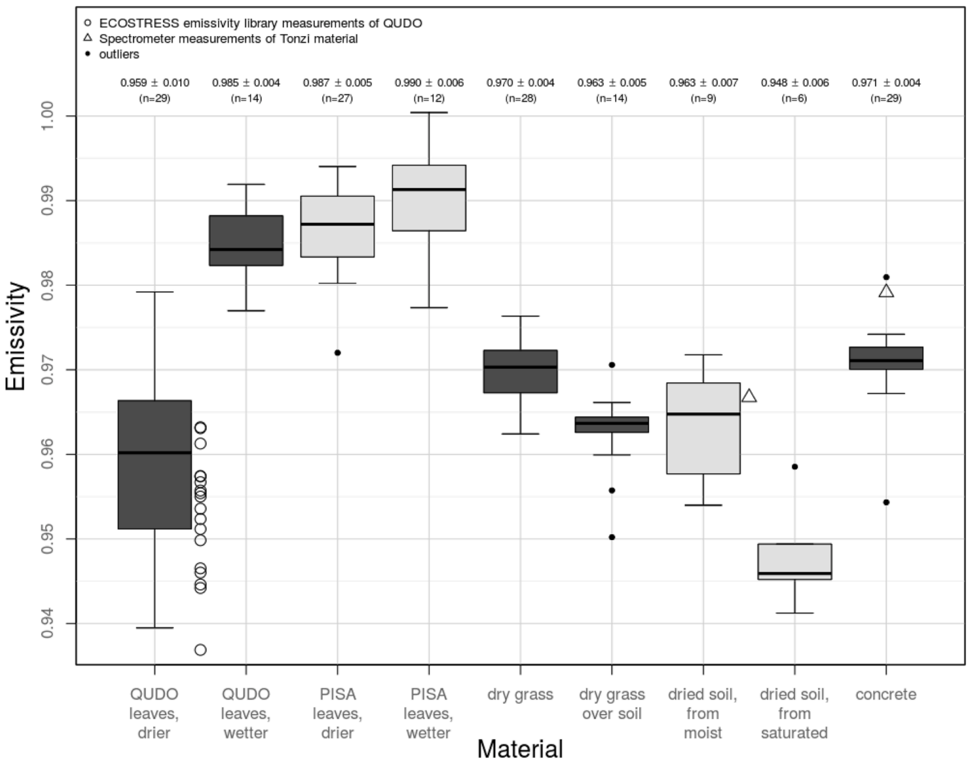

Fig. 7. Emissivity box measurements of different ecosystem components, shown with means ±1 standard deviation and sample size n. "QUDO" is *Q. douglasii* and "PISA" is *P. sabiniana*. Tree leaves were collected on December 3, 2019 and measured the next day ("wetter") and again on December 17 ("drier"); in the interim time, they were stored in a refrigerator in bags with wet paper towels. Both soil samples were fully oven-dried, but the soil dried "from moist" was rougher and less shiny than the soil dried "from saturated".

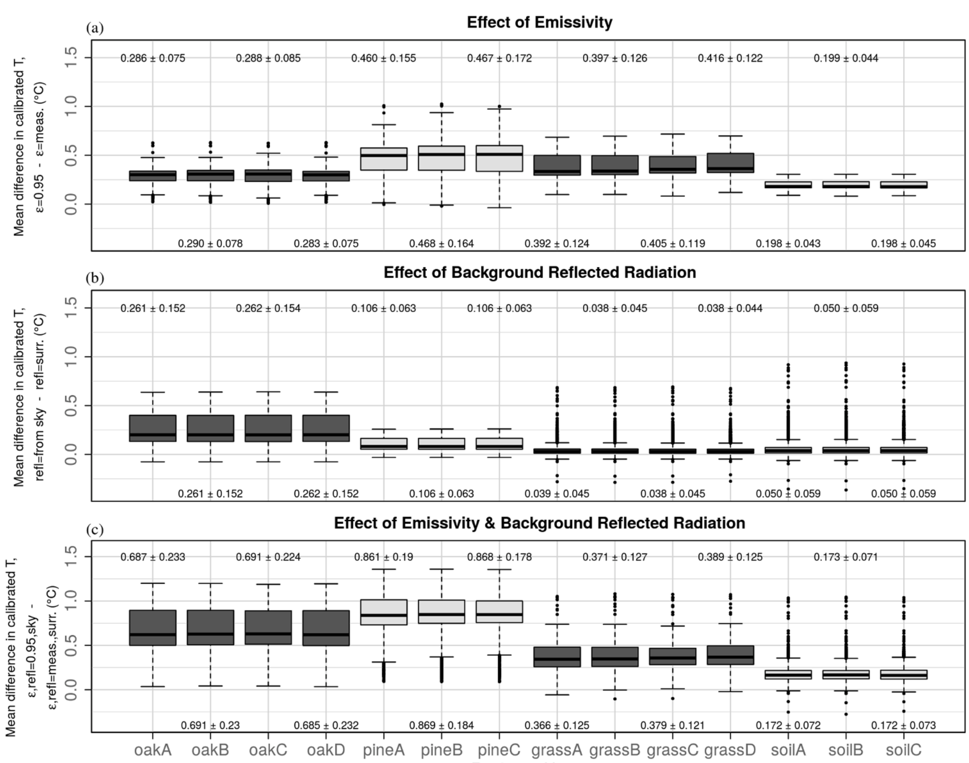

Fig. 8. Differences in calibrated target temperatures of each region of interest, given calibration choices about emissivity (0.95 or as measured by the emissivity box) and the source of Φ_{refl} (sky only or surroundings). All calibrations considered the enclosure window and used overstory air temperature and relative humidity measurements. Panel (a) shows the difference in calibrated temperatures under the assumption that all emissivities = 0.95 vs. when emissivities are as measured by the emissivity box (Φ_{refl} is from surroundings); panel (b) shows the difference in calibrated temperatures assuming that Φ_{refl} is from the sky only vs. from surroundings (emissivities are as measured); panel (c) shows the differences in target temperatures attributable to both factors, assuming emissivities = 0.95 and Φ_{refl} is from the sky vs. using measured emissivities and Φ_{refl} from surroundings. Each box represents the entire five-month time series for a particular region of interest. Quantitative labels are mean ± 1 standard deviation.

$$\epsilon_{reflected,trees} = (0.5 * \epsilon_{grass}) + 0.5 * \left[(f_{pine} * \epsilon_{pine}) + (f_{oak} * \epsilon_{oak}) + \left[(1 - f_{pine} - f_{oak}) * \epsilon_{sky} \right] \right]. \tag{6}$$

In (Eqns. 5 and 6), f is fraction cover in the approximate field of view of the camera (looking NE, within 200 m, and given a 45 °viewing angle; calculated using a sharpened and classified IKONOS image). The emissivity of the sky is assumed to be 1. Note that the emissivity of clear skies is known to deviate from one, and may be reasonably estimated using air temperature and vapor pressure (Brutsaert, 1975). However, because we calculate Φ from temperature using the inversion of (Eqn. 3), we require estimates of (second-order) reflected radiation, emissivity, and, in the case of the sky, transmissivity. In our opinion, we could reasonably define these quantities for non-transmissive sources of reflected radiation (e.g. trees and grass); estimation of sky transmittance to LW radiation was outside of the scope of this research. In calculating T_{sky} as sky brightness temperature and setting $\epsilon_{sky} = 1$, we avoid errors associated with determining T_{sky}, and accrue error associated with temperature to Φ (thermal energy) conversion. Preliminary calculations suggest that this is preferred: if we apply calculated sky emissivity and assume sky transmissivity to LW radiation is 1, magnitudes of the mean differences between camera and reference measurements of the concrete panel increase by a fractional degree. However, additional research on this topic is warranted.

We measured the emissivity of each non-sky component of the ecosystem and the reference panel using the two-lid emissivity box method (Rubio et al., 1997, 2003; Appendix C), and we corroborated the results with Nicolet 520FT-IR Spectrometer (Thermo Fisher Scientific, Waltham, MA, USA) measurements of the panel and dry soil (measured for this project), as well as *Q. douglasii* leaves (published in the ECOSTRESS spectral library v. 1.0, Baldridge et al., 2009; Meerdink et al., 2019). For consistency, because we did not have spectrometer measurements for every component of interest, we used mean emissivity box measurements for image calibrations. We considered oak and pine emissivities to be the averages of the mean "drier" and mean "wetter" values, dry grass emissivity to be the average of the mean dry grass only and mean dry grass-over-soil values, and soil emissivity to be the average of the mean of two average dried soil emissivities.

To determine the theoretical importance of considering variable ecosystem component emissivities and reflected radiation from non-sky surroundings, we applied (Eqn. 4) to a range of plausible emissivities and values of reflected radiation. To quantify the on-the-ground relevance of emissivity and reflected radiation at our site, we calibrated our images in four different ways: using measured emissivities and considering reflected radiation from all relevant surroundings, using measured emissivities and considering reflected radiation from the sky only, defining vegetation and soil emissivities to be 0.95 (e.g. the FLIR default value) and considering reflected radiation from all surroundings, and defining vegetation and soil emissivities to be 0.95 and considering reflected radiation from the sky only.

2.4.2. Mixed pixels

Given the potential for large temperature differences among the different components of an open-canopy ecosystem, the influence of mixed pixels must also be considered. When imaging in a closed-canopy ecosystem, the vegetation is typically sufficiently dense that the background is invisible to the sensor, and a small field of view shift would likely result in imaging a slightly different part of the canopy (though care should be taken if shifts result in imaging wood rather than leaves or different species). In contrast, vegetation in an open-canopy system is often relatively sparse, and a shift in a heterogeneous scene would more easily result in the inclusion of a component in the region of interest (ROI) which is quite different from the intended target (the addition of dry grass, for example, to a canopy ROI).

To isolate the issue of mixed pixels from the issues of emissivity and background reflected radiation, we assumed equal component emissivities for our quantification of the effect of mixed pixels on measured temperatures:

$$T_{mixed} = \left(\frac{\left[f_{background} * \sigma * T^4_{background} \right] + \left[\left(1 - f_{background}\right) * \sigma * T^4_{target} \right]}{\sigma} \right)^{(1/4)}, \tag{7}$$

where all temperatures (T) are in K, f is the (typically unknown) fraction of pixel which is background (i.e. non-target), and σ is the Stefan-Boltzmann constant ($\mathrm{Wm^{-2}K^{-4}}$).

To assess the theoretical effect of mixed pixels, we applied (Eqn. 7) to evaluate how the temperature of theoretical mixtures diverges from the temperature of the intended target. We then contextualized those theoretical results by quantifying the differences of concurrent temperatures of the various ecosystem components at our study site.

2.4.3. Pixel dimension

Distance of a target from the camera defines the geographic area covered by a thermal image pixel (Eqn. 8):

$$\text{Side length of square pixel} = \frac{d * tan(\theta/2)}{n_x/2}, \tag{8}$$

where side length is in meters, d is distance from the camera to the target (m), θ is the lens angle (in radians; in our case $45\pi/180$), and n_x is the number of pixel columns in the image (320, in the case of the FLIR325sc). Though more area is imaged per pixel for more distant targets, energy per area is consistently measured regardless of distance, as measurement area and signal attenuation perfectly balance, according to the inverse-square law. However, spatial aggregation may change the distribution of measured temperatures, as larger pixels make it less likely that the portion of the target falling within a pixel is atypical (Faye et al., 2016). This issue is likely to be most relevant in an open canopy system, in which the ability to see across relatively long distances and through the canopy to the ground means that regions of interest are variably distant. To quantify the influence of pixel size, we assessed the effect of spatial aggregation on the minima, maxima, 5th percentile, 95th percentile, mean, and standard deviations of the ROIs imaged at our study site. We also report results of pixel size simulations, in which we created theoretical regions of interest and compared their distributions of pixel temperatures as we spatially aggregated them, in Appendix F.

2.5. An opportunity provided by thermal imaging in an open-canopy system: The two-source energy balance model (TSEB)

To (i) contextualize the combined effects of variable background radiation and emissivity, (ii) emphasize the importance of temperature differences among ecosystem components, and (iii) demonstrate an opportunity associated with thermal camera deployment in an open-canopy system, we used thermal camera measurements to drive the two-source energy balance model (TSEB, Kustas and Norman, 1999; Li et al., 2005; Norman et al., 1995). Given radiometric surface temperatures(s) and a suite of canopy structure and meteorological variables, TSEB estimates sensible and latent energy exchanges between the soil, canopy, and atmosphere (see Appendix D for details). It provides an estimate of fluxes independent from eddy covariance measurements.

We ran TSEB in five configurations, which differed in their inputs of radiometric temperature (Table 1; note that we call T_S "substrate temperature" rather than "soil temperature," as is more common in the literature, because we consider both dry grass and soil for this input.)

We applied these configurations to answer four main questions:

1. What is the effect of the emissivity and background reflected radiation corrections (Section 2.4.1) on TSEB model accuracy? (Compare configurations 1 and 2.)
2. What is the effect of different choices of substrate (bare soil vs. dry grass) on TSEB model accuracy? (Compare configurations 2 and 3.)
3. How do the camera's concurrent measurements of T_C and T_S, which obviate the need for their approximation using a single radiometric surface temperature measurement, affect TSEB model accuracy? (Compare configurations 3 and 4.)
4. How can thermal camera data elucidate plausible micro-scale variability in energy fluxes? (Apply configuration 5 for 100 times; the output of the procedure is a distribution of sensible heat flux at each time step.) For these analyses, we selected randomly from grass rather than soil pixels because there were so few soil pixels.

We applied TSEB version 2T (for configurations 1, 2, 3, and 5) and version PT (for configuration 4) in Python (Python Core Team, 2020), with minor modifications to the radiative budget code to allow direct input of measured ground heat flux and net radiation (Nieto et al., 2019, 2020). We applied TSEB at half-hourly time steps when the net radiation was > 0. The canopy height parameter was defined as an average of mean oak height and mean pine height according to a 2018 ground survey of 288 oaks and 60 pines (Fig. 1b), weighted by the proportions of those species in the tower footprint for the period studied (Hsieh et al., 2000). LAI was derived from images taken by a zenith-oriented digital camera (Canon PowerShot A570 IS, Tokyo, Japan; Ryu et al., 2012). Otherwise, to clarify the utility of the thermal camera data and the relevance of thermal image calibration choices rather than possible tuning procedures, all inputs were as standard as possible and there was no data filtering.

To assess TSEB model results, we compared model estimates with sensible heat fluxes measured by the eddy covariance instrumentation and reported by Ameriflux; we focused comparisons on sensible heat due to tower energy budget non-closure. Given the sources of input data, we expected that TSEB model results (which are not spatially-explicit) were generally relevant to the area surrounding the flux tower. To check the assumption that the camera measurements were comparable to measurements from the tower footprint, we compared our bulk radiometric surface temperature (T_R) from the mean camera-measured canopy temperature (T_C) and soil temperature (T_S, Eqn. D.1) with $T_{R_{radiometer}}$, derived from the tower-mounted four-way radiometer (field of view: 180 degrees; see Appendix D for results). In calculating $T_{R_{radiometer}}$, we used oak, pine, and grass emissivities from the surface, weighted by their approximate abundances in the tower footprint. We considered reflected radiation to be from the sky.

3. Results and discussion

3.1. FLIR Accuracy and calibration

3.1.1. Imaging the reference panel

Each of the parameters required to convert the FLIR's raw signal into temperature (Eqns. 2 and 3) was reported, measured, or calculated, with the exception of ϵ_{sky}, which was assumed to be unity (see Appendix A for detail); there was no statistical tuning. There were, however, calibration choices associated with the source of the reflected energy, the location of the temperature and relative humidity measurements, and the presence or absence of an enclosure window. Given the physical realities, it is most reasonable to include the window and to consider reflected energy from all relevant surroundings (not just the sky). Regarding micrometeorological measurement location, the comparisons between the IRT/TCs and the FLIR measurements suggested that the air mass between the camera and the panel is best characterized by the overstory micrometeorological measurements (Appendix E, Appendix F).

On average, both the IRT and the TC measurements were cooler than the FLIR, but the root mean square (RMSE; 1.75 °C for IRT, 1.59 °C for TCs), mean absolute (MAE; 1.63 °C for IRT, 1.19 °C for TCs), and mean bias errors (MBE, 0.94 °C for IRT, 1.15 °C for TCs) for both comparisons were within the FLIR A325sc reported ±2° C accuracy (Fig. 5, Table 2). Separating the daytime (incoming SW radiation > 0 W/m^2) and night-time comparisons, we found that the night-time differences between the FLIR measurements and the TC and IRT references were more consistent than the daytime differences (standard deviation of FLIR - IRT was 1.64 °C during the day and 0.30 °C at night; standard deviation of FLIR - mean TC was 1.29 °C during the day and 0.39 °C at night). Overall error metrics were not decisively different, however: RMSE, MAE, and MBE were lower for the FLIR - IRT comparison during the day, and lower for the FLIR - mean TC comparison at night (Table 2).

The largest differences between FLIR and reference measurements were at times of high light, during which the FLIR typically measured warmer than the TCs and cooler than the IRT (Fig. 5, Appendix E). When incoming SW was in its highest quartile, mean FLIR - IRT was -1.11 °C, and mean FLIR - TC was 2.27 °C. These disparities are likely partially caused by the different measurement locations of the TCs, IRT, and FLIR. In conditions of high light, the surface of the panel was likely warmer than the subsurface, and the panel experienced higher thermal heterogeneity associated with dappled light and shadow (the Pearson correlation coefficients between incoming SW radiation and the range of FLIR concrete panel pixel temperatures and of the four thermocouple measurements was 0.71, and 0.79, respectively). The TCs, which were within the panel and covered by a thin layer of concrete putty, may have been correctly cooler than both the FLIR and the IRT under these conditions. While the IRT and the FLIR are both radiative instruments that measure surfaces, and while we assumed the same panel emissivity and reflected radiation for both, their measurement footprints were different. The IRT's footprint was similar in size to a single FLIR pixel, and the FLIR panel measurement we report was the mean of six pixels. No single FLIR pixel was in clearly better agreement with the IRT than the others (data not shown), so it is most likely that the IRT footprint covers portions of multiple FLIR pixels. We hypothesize that the seasonality of the FLIR - IRT differences in high light conditions may be associated with seasonally shifting patterns of light and shade on the panel, but additional data would be required to test this hypothesis. Given the essentially identical reflected energy and emissivity inputs for FLIR and IRT measurements, measurement disagreements must be associated with mis-specification of air mass or window corrections, with possible confounding of camera measurements by (minimal) IRT infrastructure in the camera's view, and/or with bias in the sensors themselves (Eqn. 2). It is likely that all of these contribute.

The daytime FLIR - IRT difference was significantly associated with air temperature, incoming SW radiation, hour, and month, and the night-time difference was associated with air temperature, relative humidity, wind speed, hour, and month (Tables E2 and E3). Day and night FLIR - TC_{mean} differences were similarly related to environmental covariates as their FLIR - IRT counterparts, with the notable exception that higher incoming SW increased FLIR temperatures relative to the TCs, whereas it decreased FLIR temperatures relative to the IRT. Daytime FLIR - TC_{mean} also had a relationship with wind speed, and the night-time association with relative humidity was positive (see Appendix E for multiple regression model details and diagnostics). In all cases (day and night, for both references), higher air temperature was associated with warmer FLIR measurements, compared to the reference measurements. Overall, environmental conditions explained a considerable portion of the FLIR - IRT difference (compare model log likelihood and mean residual standard error with those of an intercept-only model, which includes no environmental covariates), suggesting that statistical models could be used to adjust calibrated thermal camera measurements.

Temperature measurement differences among the four TCs (the median difference between the maximum and minimum thermocouple measurements was 0.40 °C, mean = 0.99 °C, SD = 1.15 °C; no formal cross calibration was performed) and between the IRT and the TCs (median difference between the average of the thermocouple measurements and the IRT was 0.97 °C, mean -0.21 °C, SD 2.30 °C) suggest that some of the discrepancy may not be attributable to the camera. To our knowledge, this is the only study characterizing the error of comprehensively calibrated thermal images from a FLIR A325sc deployed outdoors. The errors and biases reported here are comparable to those obtained by empirical correction (Kim et al., 2018). Because the reference panel was relatively distant from the camera and had the potential to be thermally heterogeneous, we expect that these errors are broadly representative of errors that would be present when imaging natural ROIs.

3.1.2. Effect of the enclosure window

The mean difference in the calibrated temperature of the concrete panel when the window was considered versus when it was not considered was 0.41 °C, with peaks at approximately 0.2 °C and 0.8 °C corresponding to conditions of low and high incoming SW radiation (Fig. 6). For over 99.9% of images, calibrations considering the window were warmer, despite the fact that window temperatures were 1.25 - 7.71 °C higher than air temperatures (mean difference 4.1 °C; standard deviation 1.47 °C). While the inclusion of a Φ_{win} term subtracts energy from the apparent target temperature (Φ_{target}, Eqn. 2), the presence of a window also introduces the window reflection (R_{win}) and transmission (τ_{win}) terms. The effect of $\tau_{win} < 1$ to increase Φ_{target} nearly always outweighed the effect of Φ_{win} to decrease Φ_{target}.

When the window was omitted from the calibrations, the FLIR measurements of the concrete panel's temperature had a lower RMSE compared to the thermocouples (RMSE = 1.18, MAE = 0.87, MBE = 0.75 °C) but slightly higher RMSE compared to the IRT measurements (RMSE = 1.81, MAE = 1.67, MBE = 0.54 °C; compare results to Fig. 5). Despite these mixed results, we advocate for a window correction because the error is systematic and associated with environmental conditions (Fig. 6). The correction requires measuring window temperature with a thermocouple and estimating window reflectance and transmittance (and therefore emissivity) from company-provided curves. When the Φ_{win} term is omitted from (Eqn. 2) and $\tau_{win} = 1$, we expect that calibrated target temperatures will consistently be biased low by a fraction of a degree.

When measuring the window temperature is untenable, we suggest that assuming $\Phi_{win} = \Phi_{air}$ is more realistic than assuming $R_{win} = 0$ and $\tau_{win} = 1$ (i.e. no window). In the former case, the calibrated temperatures would be warmer than if window temperature were measured by only a mean of 0.11 °C (SD = 0.032 °C). We expect that this difference would decrease as window and air temperatures converge in cooler conditions.

3.2. Challenges of thermal imaging in an open-canopy system

3.2.1. Background radiation and emissivity

Measurements of emissivity with the emissivity box agreed reasonably with measurements from the Nicolet thermal spectrometer and the ECOSTRESS emissivity library (Fig. 7). The mean emissivity of all vegetation samples was above 0.95, and was variable according to water content. Pine needles had the highest emissivity ($\epsilon = 0.988$, including both drier and wetter samples), followed by recently-harvested oak leaves ($\epsilon = 0.985$), and dried grass ($\epsilon = 0.966$, including all samples); soil dried from saturation had the lowest emissivity ($\epsilon = 0.947$). For context, in this ecosystem, calibration of a target in the concrete panel's position with emissivity of 0.988 vs. 0.947 results in a mean temperature difference over the 5-month study period of -0.526 °C (lower-emissivity target is warmer, SD = 0.263 °C).

At our site, the effect of using measured emissivity in the calibrations was largest on pine calibrations and smallest on soil calibrations (Fig. 8) because the measured emissivities of those two ecosystem components were farthest and closest to 0.95, respectively ($\epsilon_{pine} = 0.988; \epsilon_{soil} = 0.955$, Fig. 7). Following the same logic, one might expect that the effect of using measured emissivity should be higher for oak ($\epsilon_{oak} = 0.972$) than for grass ($\epsilon_{grass} = 0.966$); however, this was not the case because the Φ_{total} associated with grass was sufficiently higher than Φ_{total} associated with oak (likely a function of grass senescence, low water content, and low atmospheric coupling, Rotenberg and Yakir, 2010). Regarding reflected background radiation, inclusion of non-sky surroundings in Φ_{refl} had a larger effect on the calibrated temperatures of oak and pine than of soil and grass because tree surroundings included radiation from both above and below, whereas grass/soil reflected radiation came entirely from above in our formulation, and therefore included a comparatively greater proportion of sky. Within overstory (pine/oak) or understory (grass/soil) groups, the effect of the background radiation was higher for the component with the lower emissivity (Fig. 8b). Results from different ROIs of the same type were remarkably consistent, suggesting that they are relatively insensitive to distance from the camera/pixel size (Fig. 8).

Overall, increasing emissivity and including non-sky surroundings in reflected background radiation almost universally decreased the calibrated target temperature, but only by a small amount. Considering measured emissivity and reflected radiation together, the differences in calibrated temperatures in this system were up to 1.36 °C (for pine), but were generally less than a degree, and were often less than half a degree for components with a measured emissivity closer to 0.95 and for which a substantial portion of reflected radiation came from the sky. Because Φ_{refl} contributes a smaller proportion of Φ_{total} when ϵ_{target} is higher (Eqn. 2), the relatively high component emissivities at the US-Ton ecosystem decreased the possibly-confounding effects of variable reflected radiation (Fig. 8).

Theoretically, emissivity and the source of Φ_{refl} have the potential to be considerably more influential. At the canonical $\epsilon_{target} = 0.95$, a difference in reflected radiation corresponding to 20 °C (a conservative estimate of the difference in temperature between the sky and terrestrial components of the ecosystem), would result in a 0.61 - 1.44 °C difference in the calibrated temperature (higher when $T_{measured}$ is lower and Φ_{refl} is higher, Fig. 9). A difference in reflected radiation of 10 °C would result in a 0.28 - 0.69 °C difference in calibrated temperature, and a difference in reflected energy of 30 °C would result in a 0.97 - 2.27 °C difference. It is not unreasonable, however, to assume that component emissivity in some systems is considerably lower than 0.95 (Meerdink et al., 2019, Appendix C). In the case where $\epsilon_{target} = 0.90$, a reflected energy difference of 20 °C would result in a 1.26 - 3.11 °C difference in calibrated temperature.

3.2.2. Mixed pixels

The effect of unintended imaging of a background component within a target pixel is larger when (i) the background is a greater proportion of the pixel, and (ii) the temperatures of the intended target and the background diverge (Fig. 10). Also, as the background temperature increases, a smaller change in its temperature results in a larger change in $T_{mixed} - T_{target}$, according to the nonlinear Stefan-Boltzmann relationship between temperature and energy (Fig. 10). Though it is impossible to determine which pixels are mixed using a thermal camera alone, the temperature differences between components allowed us to calculate the influence of potential mixtures on calibrated temperatures.

In our study area, as in many open-canopy systems, the sparsity of vegetation would make mixed pixels common, and the large divergence of ecosystem component temperatures (Fig. 11) would result in dramatic effects of mixed pixels on temperature estimates. The most confounding mixed pixels would be those in which a canopy component mixes with a ground component or with the sky. The distributions characterizing the difference between oak and grass temperature and oak and soil temperature have long tails (Fig. 11; grass temperature was 17.1 °C warmer to 7.26 °C cooler than oak, and soil temperature was 24.9 °C warmer to 6.33 °C cooler than oak). In the case that the unintended fraction of grass or soil is 20% and differences are at their first quartile (-5.41 °C for grass, -6.76 °C for soil), a mixed pixel would overestimate oak temperature by more than 1 °C (depending on the exact temperature values). In a more extreme case, if the temperature difference were -20 °C, even a 5% pixel impurity would change the calibrated oak temperature by 3.00 °C (if true oak temperature were 20 °C), by 2.25 °C (if true oak temperature were 30 °C), or by 1.89 °C (if true oak temperature were 40 °C). Conversely, if the fraction of grass or soil were relatively low (on the order of 5%) and the temperature difference were at its mean, a mixed pixel would overestimate oak temperature by less than 0.5 °C.

Mixing of oak with a sky background would also have a large effect on the calibrated temperatures. Over the five month study period, the mean difference (± standard deviation) between oak temperature and sky brightness temperature was 20.28 (± 4.41) °C. If an otherwise-oak pixel comprised 20% sky and the temperature difference were at its mean, a mixed pixel would underestimate true oak temperature by about 2 °C. Conversely, if the fraction of sky were only 5%, a mixed pixel would typically underestimate oak temperature by less than 0.5 °C.

If the mixture in a pixel were of canopy components (oak/pine) or understory components (grass/soil), then the calibrated temperatures would be considerably more accurate. Oaks and pines had the most similar temperatures among ecosystem components (mean value of oak - pine temperature $\pm$ 1 standard deviation was -0.71 $\pm$ 0.99 °C, minimum was -3.76 °C, maximum was 2.99 °C). If pine comprised 20% of an otherwise-oak pixel and oak and pine temperatures differed by their maximum 3.76 °C, T_{mixed} would differ from T_{target} by 1.01 °C, in the most extreme circumstance measured. More typically, when the difference between oak and pine temperature was at its mean, T_{mixed} would differ from T_{target} by closer to 0.15 °C. Likewise, grass and soil had comparatively similar temperatures (the mean of grass - soil temperature was -3.16 °C with a standard deviation of 3.57 °C). A grass pixel that included 20% soil, given that mean temperature difference, would result in grass temperature overestimation of about 0.75 °C.

Overall, the impact of mixed pixels in our system would be largest when surface temperature and incoming shortwave radiation is high, which is associated with diverging component temperatures (Fig. 11). Interestingly, from the perspective of measuring oak temperature, the confounding effect of another component could be in either direction, because high incoming shortwave radiation is associated with pine and sky temperatures which are generally lower than oak temperatures, and with grass and soil temperatures which are generally higher. It is important to note that while ecosystem thermal heterogeneity may be a nuisance from a calibration perspective, the thermal camera's ability to capture such heterogeneity affords it the potential to address diverse and important questions in biometeorology (e.g. energy balance), plant ecology and physiology (e.g. thermal niches, photosynthesis and respiration rates, etc.), animal ecology (e.g. microhabitats), and rangeland science (e.g. temperature refugia) – among others.

3.2.3. Pixel dimensions

The regions of interest (Fig. 3) were located between 27 m (nearest oak) and 122 m (farthest pine) from the camera; square pixel dimensions ranged from 0.070 - 0.32 m, which represents a twenty-fold variation in pixel area. Nearly all oak, grass, and soil ROIs had significantly lower temperature maxima and significantly higher temperature minima as pixel size increased (Faye et al., 2016); pine ROI minima and maxima

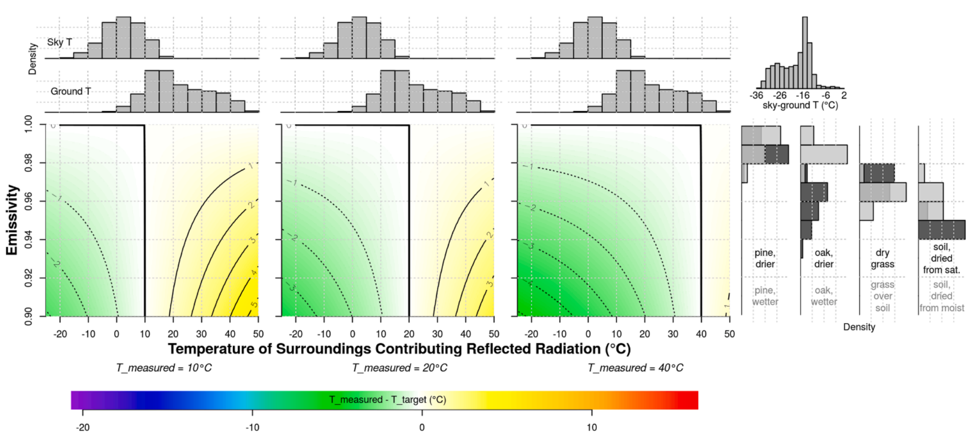

Fig. 9. Theoretical heat maps showing the effects of target emissivity and the temperature of the surroundings contributing reflected radiation on $T_{measured}$ - T_{target}, the difference between what the sensor sees and the true temperature of the target. Histograms are data from US-Ton, for context. Sky temperature and ground temperature are calculated from tower radiometer measurements of incoming and outgoing LW radiation according to Eqn A.6; emissivity measurements are from the emissivity box. Color bar is the same on all heatmap figures. (The reader is referred to the web version of this article for colors.)

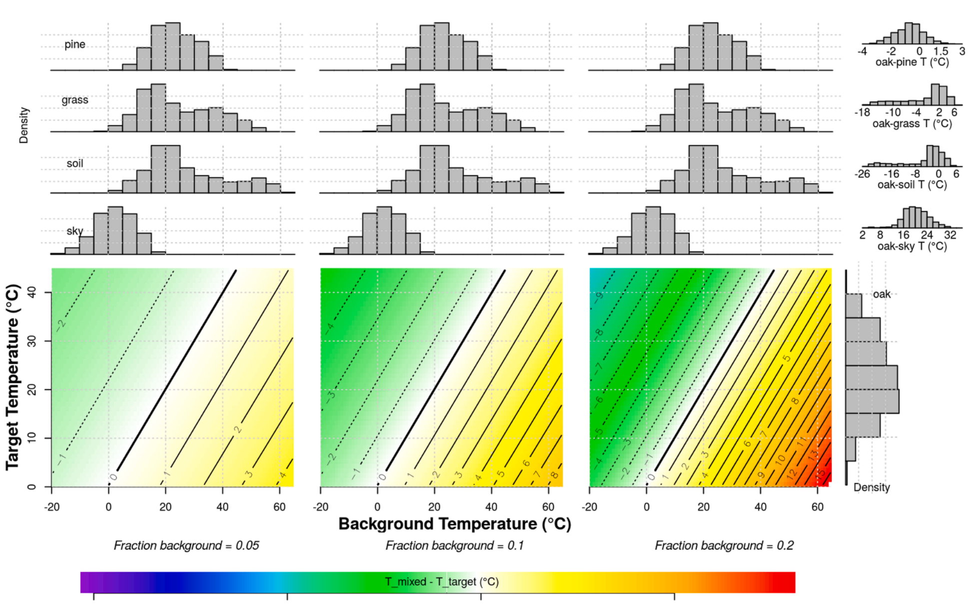

Fig. 10. Theoretical heat maps showing the effects of background temperature and fraction background on the over- or under-estimation of the target temperature, quantified as the difference between the mixed pixel temperature, T_{mixed}, and the true target temperature, T_{target}. Histograms are data from US-Ton, for context, assuming that the focus region of interest is oak, and any other component would be "background." Color bar is the same on all heatmap figures. (The reader is referred to the web version of this article for colors.)

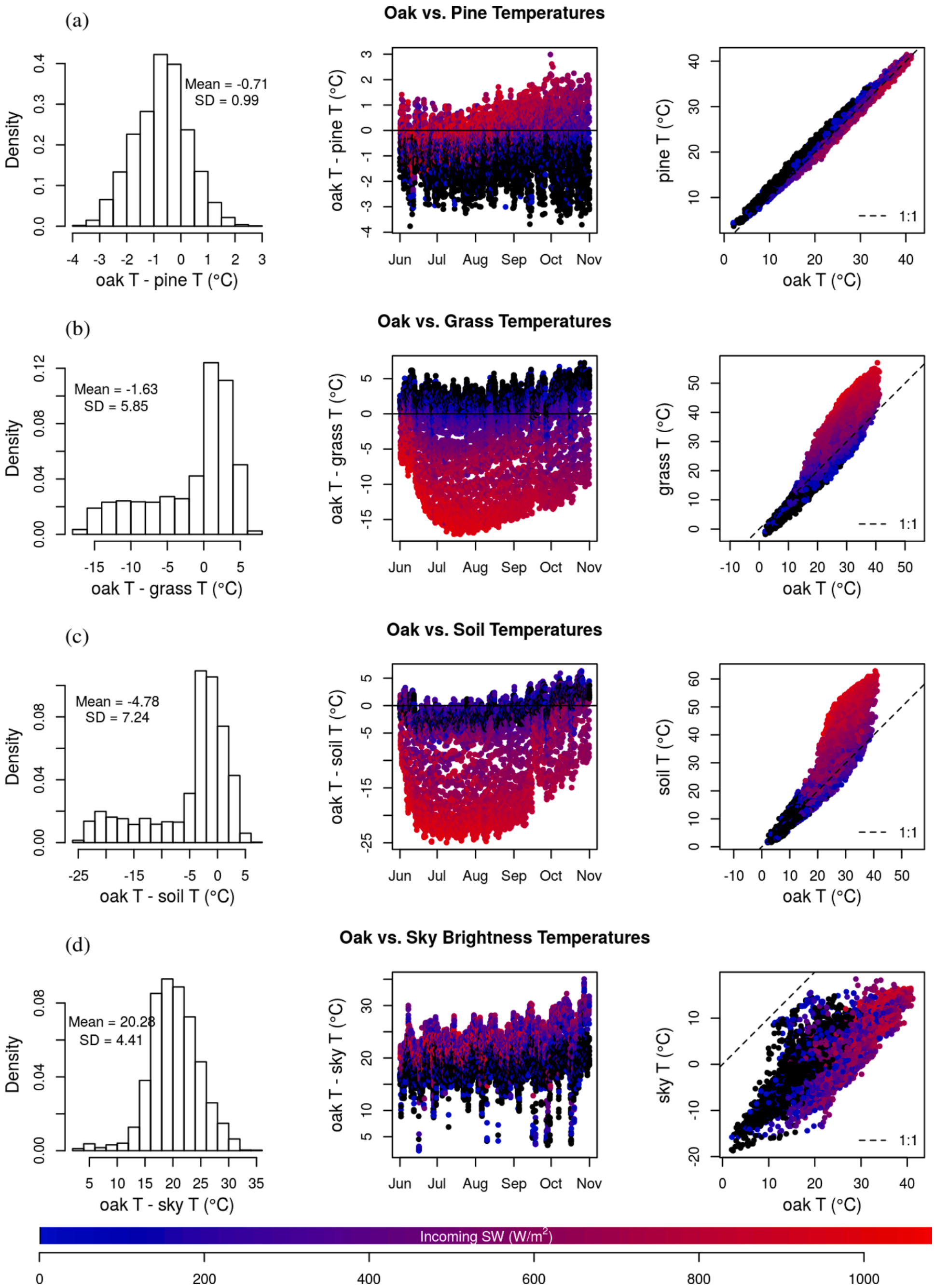

Fig. 11. Comparison of half-hourly mean oak temperatures with (a) pine temperatures, (b) grass temperatures, (c) soil temperatures, and (d) sky brightness temperatures (all calibrated from FLIR camera measurements except for sky temperatures, which were measured by the tower-mounted radiometer). Pixel sizes were aggregated to be equivalent at 31.6 cm before comparisons. Colors are scaled according to incoming shortwave radiation; black is incoming SW = 0 W/m^2, blue is lower radiation, and red is higher. Please see Appendix F for pine/grass, pine/soil, and grass/soil comparisons. (For interpretation of the references to color in this figure legend, the reader is referred to the web version of this article.)

were less affected by spatial aggregation, though this result is likely associated with the shorter data domain for pine (Fig. 12). Applying the linear fits to standardize comparisons for pixel sizes of typically near ROIs (e.g. 30 m from the camera, pixel size = 7.8 cm) vs. typically far ROIs (e.g. 120 m from the camera, pixel size = 31 cm), differences between oak ROI maxima were 0.52 - 1.33 °C, between grass maxima 0.10 - 1.41 °C, between soil maxima 0.79 - 1.51 °C, and between pine maxima 0.0033 - 0.045 °C. Given the same standardization, differences between oak ROI minima were -0.14 - -0.48 °C, between grass minima -0.094 - -0.39 °C, between soil minima -0.37 - -0.97 °C, and between pine minima -0.059 - 0.020 °C. In contrast, means, standard deviations, and fifth and ninety-fifth quantile values varied little. Even in cases for which the pixel dimension vs. mean temperature slope was significantly different from zero (oakA, oakC, pineB, and grassC), the slope was shallow, and the difference between 30 m and 120 m ROI means was always less than 0.038 °C (Fig. 12).

3.2.4. *Summary*

Thermal imaging considerations with the potential to be particularly relevant in open-canopy ecosystems include variable target emissivity, reflected radiation from diverse surroundings, confounding by mixed pixels, and diverse pixel sizes within a scene. At our study site, consistently high emissivities minimized the influence of reflected radiation, whereas large temperature differences among ecosystem components emphasized the need to avoid mixed pixels (Table 3). When comparing temperatures of ROIs with different pixel sizes, summary statistics were more reliable than extreme values. In addition, we included the enclosure window in our calibrations (Eqn. 2), corrected emissivities according to instrument spectral response functions (Appendix C), and considered the relevance of over vs. understory air temperature and relative humidity measurement location (Table 3).

While our focus was on open-canopy ecosystems, many of these considerations are also likely to be relevant to closed-canopy ecosystems. In particular, there is high potential for mixed pixels to be confounding any time there is thermal heterogeneity across ecosystem components (e.g. due to the presence of both leaves and branches). It is also possible for pixels in images of closed-canopy forests to correspond with variable geographic areas, if the camera has a shallow view angle. Enclosure window corrections and consideration of radiometer vs. IRT vs. camera spectral responses when measuring emissivity are also universally relevant.

3.3. An opportunity: Estimating sensible heat flux using thermal images

3.3.1. Improving model predictions: Input processing and choice of substrate

TSEB prediction accuracy at this site was within the limits established by similar research in open canopies (e.g. Andreu et al., 2019; Kustas et al., 2016; Nieto et al., 2019). Errors were slightly higher compared to other savanna applications (Andreu et al., 2018, 2019; Burchard-Levine et al., 2019), but this was expected given that we used a standard TSEB parameterization and performed no site-specific model calibration. TSEB prediction accuracy was also comparable to eddy covariance energy budget closure: when comparing the available energy (R_N - G) with the turbulent fluxes ($H + LE$), the MBE was 74.93 W/m^2, the MAE was 93.15 W/m^2, and the RMSE was 117.41 W/m^2). In future applications, we expect that TSEB errors would decrease if a tower footprint analysis were conducted and the area of measurement of each sensor were synchronized.

The largest improvement in predictions of sensible heat flux was associated with the direct ingestion into the model of canopy (T_C) and substrate (T_S) temperatures, compared to inputting bulk radiometric surface temperature (Fig. 13d vs. c). Over the five-month period of interest and with eddy covariance tower measurements as a reference, camera measurements of T_S and T_C decreased the RMSE of the sensible

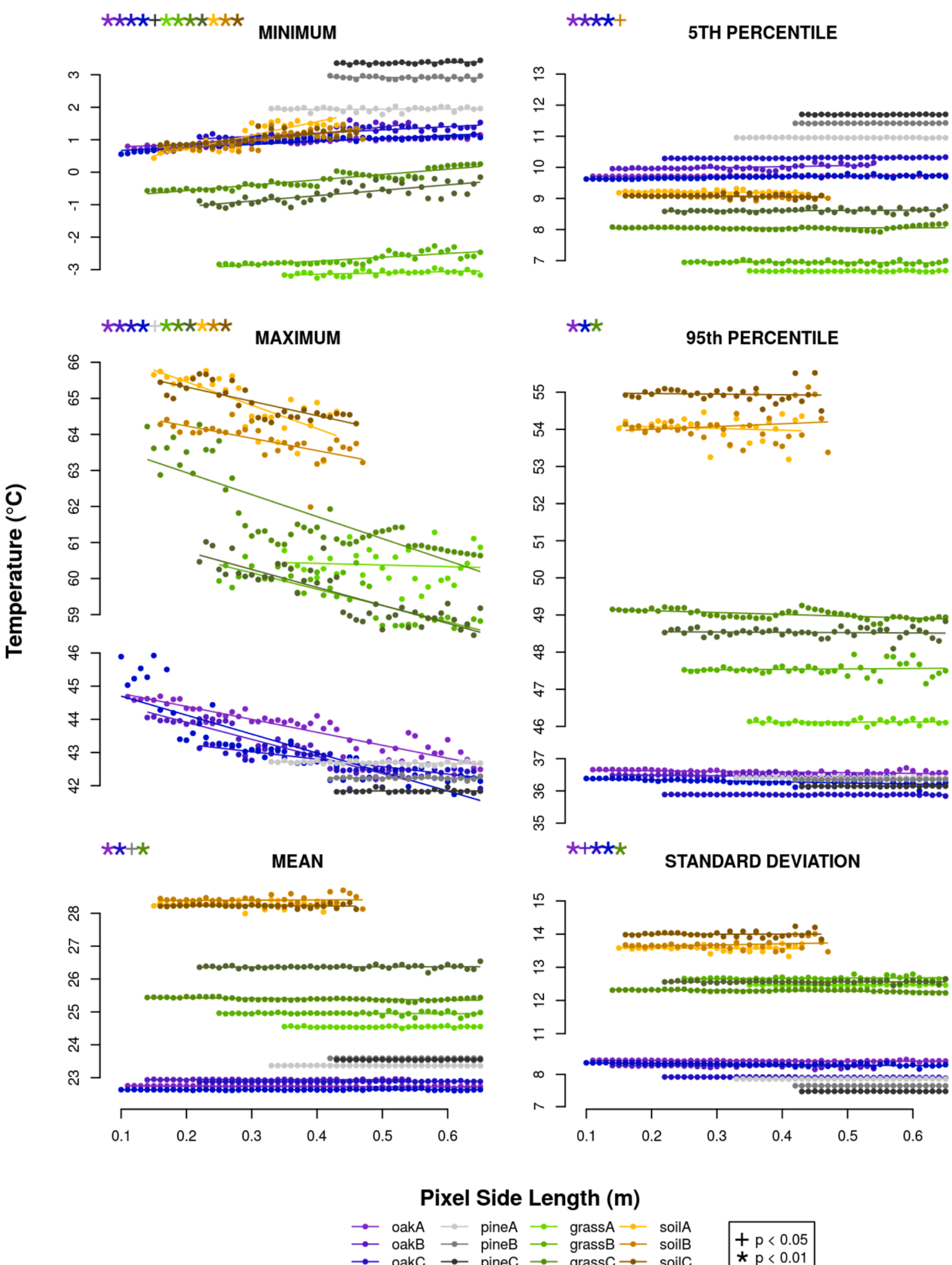

Fig. 12. Summary statistics for a thermal time series of each ROI, given different pixel sizes. Each point represents the summary for all ROI pixels over the five month study period. When there are no points at the smaller pixel sizes, it is because the ROI was too distant from the camera. When there are no points at the larger pixel sizes, it is because the ROI was too small to be aggregated. Significance symbols denote whether the slope of the line is significantly different from 0; note that significance has not been corrected for the different data domains of each ROI. (The reader is referred to the web version of this article for colors.)

Table 3
Summary of thermal image calibration priorities at US-Ton. Corrections/considerations in the first column are considered in isolation. Priority designations in the second column are rough, as results vary when corrections/considerations are applied in combination, for regions of interest with various characteristics (including temperature), and under different micrometeorological conditions. "Low" priority corrections/considerations typically change calibrated temperatures by <0.3 °C, "medium" priority corrections typically change calibrated temperatures by >0.3 but <1.0 °C, and "high" priority corrections may often change calibrated temperatures by >1.0 °C.

Correction / Consideration	Priority at US-Ton	Increasing importance as:
Target emissivity ≠ 0.95	Low - Medium	- True emissivity is farther from 0.95 - Reflected and target temperatures diverge
Reflected radiation from surroundings	Low	- Target emissivity decreases - Surroundings temperature diverges from sky temperature
Mixed pixels	High	- Fraction non-target increases - Target and non-target temperatures diverge
Pixel dimension	Low - High	- Pixel size decreases - Temperatures more heterogeneous - Values of interest more extreme
Enclosure window	Low	- Window becomes cooler - Window transmissivity decreases - Window reflectivity increases
Over vs. understory micrometeorology (Appendix F)	Low	- Distance between target and camera increases - Difference between over and understory conditions increases
Emissivity spectral response correction (Appendix C)	Low	- Instrument spectral ranges and responses diverge - Target emissivity is variable by wavelength

heat flux prediction by 26.45 W/m^2 (from 97.86 W/m^2 to 71.41 W/m^2), the MAE by 24.08 W/m^2 (from 78.33 W/m^2 to 54.25 W/m^2), and the MBE by an absolute value of 67.75 W/m^2 (from 67.04 W/m^2 to -0.72 W/m^2, Fig. 13). This was a result we expected, given that component temperature ingestion avoids the Priestly-Taylor estimation and model iteration (Andreu et al., 2015; Nieto et al., 2019; Song et al., 2016, 2020); it underscores the utility of spatially- and temporally explicit thermal data in energy balance applications.

The second largest improvement in sensible heat flux predictions was associated with using bare soil rather than dry grass as T_S(Fig. 13b vs. c).

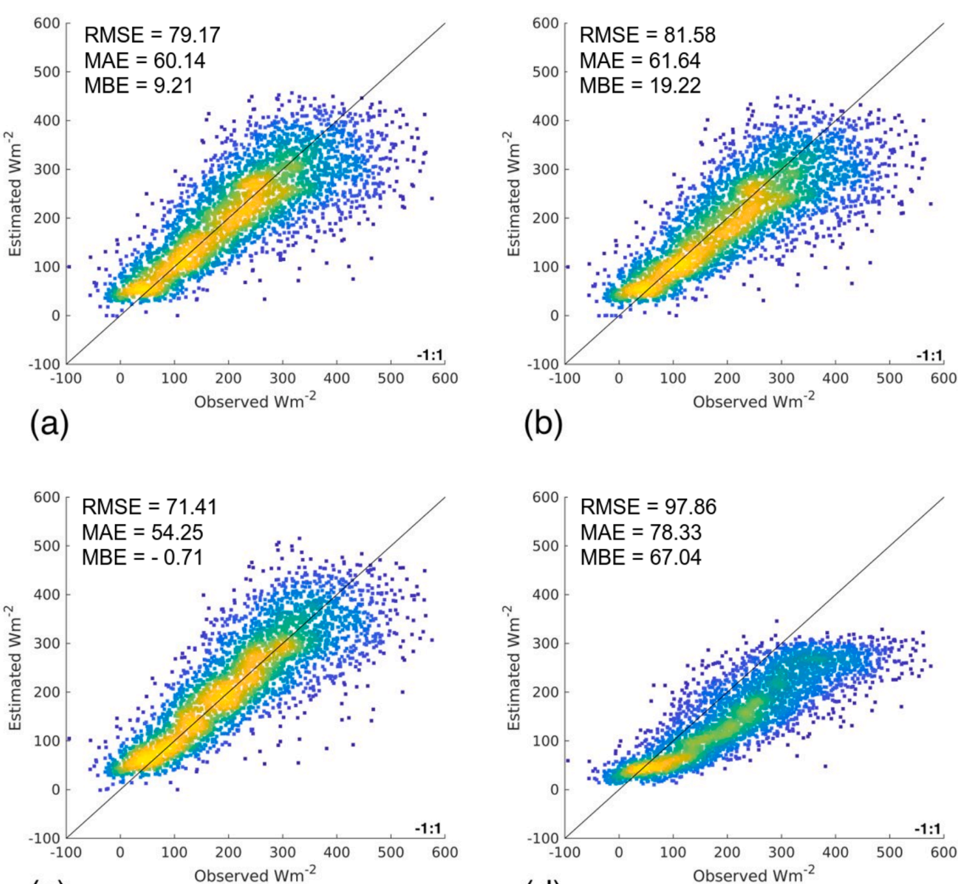

Fig. 13. Comparison of measured and estimated sensible (H) and latent (LE) heat fluxes; axes are sums of turbulent fluxes, and each data point is a daytime half hour when net radiation > 0. Plot (a) shows the results of TSEB configuration 1 (Table 1), in which T_C and T_S were calculated assuming $\epsilon = 0.95$ and $\Phi_{refl} = \Phi_{sky}$, and T_S was grass temperature. Plot (b) shows the results of TSEB configuration 2, in which T_C and T_S were calculated with ϵ as measured and Φ_{refl} of relevant surroundings, and T_S was grass temperature. Plot (c) shows the results of TSEB configuration 3, in which ϵ was as measured, Φ_{refl} considered relevant surroundings, and T_S was soil temperature. Plot (d) shows the results of the TSEB-PT simulation (configuration 4), in which T_R was an input rather than T_S and T_C. Points are colored by density (and the reader is referred to the web version of this article for colors).

With this change, RMSE improved by 10.17 W/m^2, MAE improved by 7.39 W/m^2, and MBE improved by 18.51 W/m^2. In contrast, inputting "corrected" T_S and T_C values, calibrated using emissivity measurements and Φ_{refl} values from the surroundings (Section 2.4.1), actually resulted in slightly lower TSEB accuracy (Fig. 13a vs. b; RMSE declined by 2.41 W/m^2, MAE declined by 1.50 W/m^2, and MBE declined by 10.01 W/m^2). This decreased accuracy makes sense, in light of the fact that the corrections decrease calibrated temperatures, while soil temperatures are, on average, higher than grass temperatures by 3.15 °C (SD = 3.57 °C). These results suggest that the soil temperature characterizes the lower boundary of the driving gradient for sensible heat flux more accurately than the overlying dry grass. Alternatively or additionally, bare soil could be a more thermally dominant cover than dry grass in the tower's footprint.

3.3.2. Sensible heat flux distributions

In addition to concurrent measurements of T_S and T_C, thermal cameras have the capacity to measure temperature variability within the canopy and the substrate. When driven with these variable temperatures, TSEB can estimate micro-scale variability of sensible and latent heat fluxes associated with, for example, sun/shade spots and different vertical layers of the canopy.

One hundred TSEB simulations with a single randomly-selected canopy pixel as T_C and a single randomly-selected grass pixel as T_S yielded a distribution of sensible heat flux predictions at every daytime half hour (Fig. 14a). At the half-hourly time scale, the distributions of predicted sensible heat fluxes were typically broader at midday than in the morning or late afternoon. The daily prediction variability corresponded strongly with incoming shortwave radiation, with low radiation conditions associated with decreased variability (Fig. 14b; Pearson correlation = 0.87). Seasonally, prediction variability and shortwave

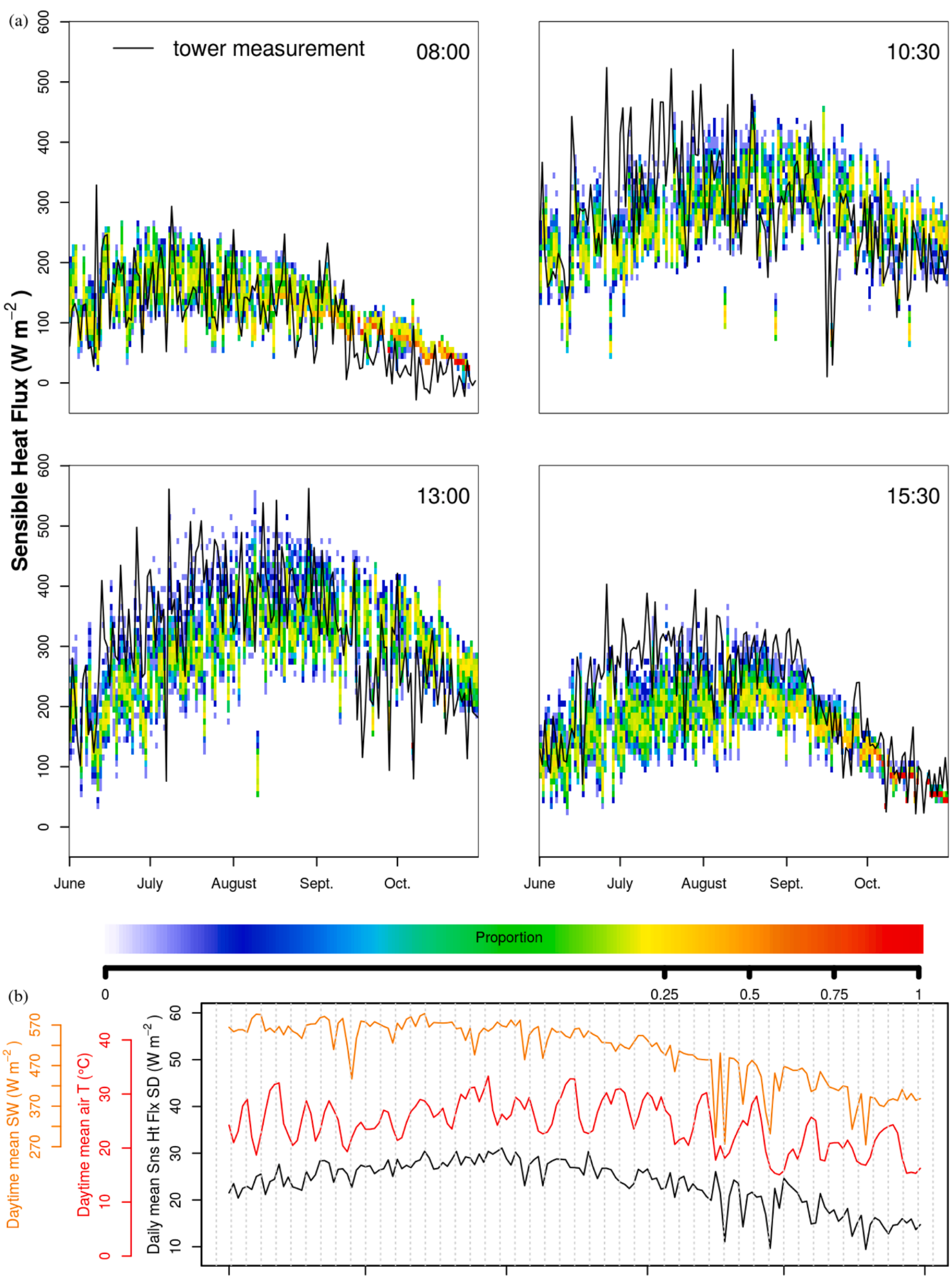

Fig. 14. Panels in (a) show the distributions of sensible heat flux predictions (TSEB configuration 5) at all 8:00, 10:30, 13:00, and 15:30 half-hours, June - October. Note the consistent underestimation of H compared to the tower measurements, in part because these simulations considered grass pixels for T_S. Panel (b) shows daily mean standard distributions of predicted daytime sensible heat fluxes compared with daytime incoming SW radiation and mean air temperature. (The reader is referred to the web version of this article for colors.)

radiation were even more tightly coupled: the Pearson correlation between a 20-day moving average of daily shortwave and predicted sensible heat flux variability was 0.96.

4. Conclusions

In our open-canopy savanna system, the effects of large temperature differences among ecosystem components dominated the effects of emissivity and reflected radiation diversity, both in calibration (mixed pixels are most confounding) and in application (choice of substrate has a larger effect on TSEB results than emissivity/reflected radiation corrections). This result highlights the value of spatially-explicit thermal measurements, which is further emphasized by the utility of multiple temperature measurements within a region of interest to produce a distribution of model predictions.

Emissivities of oak, pine, dry grass, and soil in our system were all higher than 0.95, the often-assumed value. Where these high emissivities are characteristic (in either open- or closed-canopy ecosystems), the confounding effect of variable reflecting background radiation will be comparatively minor. However, if components with lower emissivities are present, variable reflected radiation across the scene will have a considerably greater influence. To avoid that possibility, we recommend characterization of ecosystem component emissivities (e.g. via the emissivity box method, emissivity libraries, or remote sensing) when thermal imaging in open-canopy ecosystems.

Generalizing across ecosystem components and regions of interest, we found that (i) mean FLIR A325sc disagreement with independent temperature measurements was on the order of 1.7 °C (on average, images were too warm, Section 3.1.1); (ii) in conditions of high incoming SW radiation, disagreement between the FLIR and independent temperature measurements was the highest and occasionally exceeded 4 °C, though IRT and TC measurements also diverged at these times; (iii) the effect of including the enclosure window was about 0.4 °C (omitting the enclosure window made calibrations cooler, Section 3.1.2); (iv) commonly-assumed emissivity and reflected radiation conditions cooled calibrations by about 0.5 °C (Section 3.2.1); (v) mixed pixels can bias calibrations in either direction by up to several degrees Celsius (Section 3.2.2), and pixel size has an effect on extreme values of up to 1.5 °C, but little effect on mean values (Section 3.2.3). Taken together, these magnitudes of possible error have the potential to confound measurements of true temperature differences between ecosystem components of interest. However, each can also be ameliorated, for example by (i) modeling inherent error as a function of environmental conditions or comparing relative temperatures, (ii) measuring the temperature of the enclosure window, (iii) measuring emissivity, and (iv) defining regions of interest with margins in dense vegetation and/or using a co-registered visible camera to define the extent of pixel mixture.

Overall, we find that the challenges of thermal imaging in an open-canopy ecosystems considered here can be adequately addressed, thereby allowing for accurate measurement of temperatures by thermal cameras in heterogeneous open-canopy ecosystems. Spatially-explicit temperature measurements have high potential, among other applications, as inputs for energy balance models (e.g. TSEB) and to quantify temporally-resolved vegetation thermal heterogeneity (e.g. between oaks, pines, and understory grasses).

Funding

This work was supported by NASA Earth and Space Science Fellowship award NNX16AO21H to M. Johnston and P. Moorcroft, the Harvard University Department of Organismic and Evolutionary Biology, and the European Union's Horizon 2020 Research and Innovation program, Marie Sklodowska-Curie grant agreement No. 703978 to A. Andreu.

Declaration of Competing Interest

None.

Acknowledgements

The authors would like to thank Elsa Abbott for spectrometer measurements of the panel and the soil, Jonathan Franklin for suggesting a Sobel filter/FFT detection of FOV shifts, Eva Rubio for consultation on the emissivity box, Alfonso Torres-Rua for emissivity discussions, Hector Nieto for pyTSEb code and support, and Koen Hufkens, Don Aubrecht, Youngil Kim, Susan Meerdink, Tony Rockwell, and Steve Wofsy for instrumentation consultation. In addition, many thanks to two anonymous reviewers for their constructive comments.

Supplementary materials

Appendices associated with this article can be found in the online version at doi:10.1016/j.agrformet.2021.108484.

References

Anderson, M., Norman, J.M., Mecikalski, J., Otkin, J., Kustas, W.P., 2007. A climatological study of evapotranspiration and moisture stress across the continental United States based on thermal remote sensing: 1. model formulation. J Geophys Res 112 (10), D10117. https://doi.org/10.1029/2006JD007506.

Andreu, A., Dube, T., Nieto, H., Mudau, A.E., Gonzlez-Dugo, M.P., Guzinski, R., Hlsmann, S., 2019. Remote sensing of water use and water stress in the African savanna ecosystem at local scale – development and validation of a monitoring tool. Phys Chem Earth 112, 154–164. https://doi.org/10.1016/j.pce.2019.02.004.

Andreu, A., Kustas, W.P., Polo, M.J., Carrara, A., Gonzlez-Dugo, M.P., 2018. Modeling surface energy fluxes over a dehesa (oak savanna) ecosystem using a thermal based two source energy balance model (TSEB) II – integration of remote sensing medium and low spatial resolution satellite images. Remote Sens 10 (4), 558. https://doi.org/10.3390/rs10040558.

Andreu, A., Timmermans, W., Skokovic, D., Gonzlez-Dugo, M.P., 2015. Influence of component temperature derivation from dual angle thermal infrared observations on TSEB flux estimates over an irrigated vineyard. Acta Geophys 63, 1540–1570. https://doi.org/10.1515/acgeo-2015-0037.

Aubrecht, D., Helliker, B., Goulden, M.L., Roberts, D.A., Still, C.J., Richardson, A.D., 2016. Continuous, long-term, high-frequency thermal imaging of vegetation: uncertainties and recommended best practices. Agric For Meteorol 228–229, 315–326. https://doi.org/10.1016/j.agrformet.2016.07.017.

Baldocchi, D., Chen, Q., Chen, X., Ma, S., Miller, G., Ryu, Y., Xiao, J., Wenk, R., Battles, J., 2010. Ecosystem Function in Savannas: Measurement and Modeling at Landscape to Global Scales. CRC Press, Taylor & Francis Group, pp. 135–151.

Baldocchi, D.D., Xu, L., Kiang, N., 2004. How plant functional-type, weather, seasonal drought, and soil physical properties alter water and energy fluxes of an oak-grass savanna and an annual grassland. Agric For Meteorol 123 (1–2), 13–39. https://doi.org/10.1016/j.agrformet.2003.11.006.

Baldridge, A.M., Hook, S.J., Grove, C.I., Rivera, G., 2009. The ASTER spectral library version 2.0. Remote Sens Environ 113, 711–715. https://doi.org/10.1016/j.rse.2008.11.007.

Brown, H., Escombe, F., 1905. Researches on some of the physiological processes of green leaves, with special reference to the interchange of energy between the leaf and its surroundings. Proc R Soc Lond B 76 (507), 29–111. https://doi.org/10.1098/rspb.1905.0002.

Brutsaert, W., 1975. On a derivable formula for long-wave radiation from clear skies. Water Resour Res 11, 742–744. https://doi.org/10.1029/WR011i005p00742.

Burchard-Levine, V., Nieto, H., Riao, D., Migliavacca, M., El-Madany, T., Perez-Priego, O., Carrara, A., Martin, M.P., 2019. Adapting the thermal-based two-source energy balance model to estimate energy fluxes in a complex tree-grass ecosystem. Hydrol Earth Syst Sci Discuss. https://doi.org/10.5194/hess-2019-354.Preprint

Farquhar, G.D., von Caemmerer, S., Berry, J.A., 1980. A biochemical model of photosynthetic CO2 assimilation in leaves of C3 species. Planta 149 (1), 78–90. https://doi.org/10.1007/BF00386231.

Faye, E., Dangles, O., Pincebourde, S., 2016. Distance makes the difference in thermography for ecological studies. J Therm Biol 56, 1–9. https://doi.org/10.1016/j.jtherbio.2015.11.011.

Gates, D., 1968. Transpiration and leaf temperature. Annu Rev Plant Physiol 19, 211–238. https://doi.org/10.1146/annurev.pp.19.060168.001235.

Heskel, M.A., O'Sullivan, O.S., Reich, P.B., Tjoelker, M.G., Weerasinghe, L.K., Penillard, A., Egerton, J.J.G., Creek, D., Bloomfield, K.J., Xiang, J., Sinca, F., Stangl, Z.R., Martinez-de la Torre, A., Griffin, K.L., Huntingford, C., Hurry, V., Meir, P., Turnbull, M.H., Atkin, O.K., 2016. Convergence in the temperature response of leaf respiration across biomes and plant functional types. PNAS 113, 3832–3837. https://doi.org/10.1073/pnas.1520282113.

Heusinkveld, B.G., Jacobs, A.F.G., Holtslag, A.A.M., Berkowicz, S.M., 2004. Surface energy balance closure in an arid region: role of soil heat flux. Agric For Meteorol 121 (1–2), 21–37. https://doi.org/10.1016/j.agrformet.2003.09.005.

Hsieh, C., Katul, G., Chi, T., 2000. An approximate analytical model for footprint estimation of scalar fluxes in thermally stratified atmospheric flows. Adv Water Resour 23 (7), 765–772. https://doi.org/10.1016/S0309-1708(99)00042-1.

Jackson, R., Reginato, R., Idso, S., 1977. Wheat canopy temperature: a practical tool for evaluating water requirements. Water Resour Res 13 (3), 651–656. https://doi.org/10.1029/WR013i003p00651.

Kim, Y., Still, C.J., Hanson, C.V., Kwon, H., Greer, B.T., Law, B.E., 2016. Canopy skin temperature variations in relation to climate, soil temperature, and carbon flux at a ponderosa pine forest in central Oregon. Agric For Meteorol 226–227, 161–173. https://doi.org/10.1016/j.agrformet.2016.06.001.

Kim, Y., Still, C.J., Roberts, D.A., Goulden, M.L., 2018. Thermal infrared imaging of conifer leaf temperatures: comparison to thermocouple measurements and assessment of environmental influences. Agric For Meteorol 248, 361–371. https://doi.org/10.1016/j.agrformet.2017.10.010.

Kustas, W.P., Nieto, H., Morillas, L., Anderson, M., Alferi, J., Hipps, L., Villagarcia, L., Domingo, F., Garcia, M., 2016. Revisiting the paper "Using radiometric surface temperature for surface energy flux estimation in mediterranean drylands from a two-source perspective". Remote Sens Environ 184, 645–653. https://doi.org/10.1016/j.rse.2016.07.024.

Kustas, W.P., Norman, J.M., 1999. Evaluation of soil and vegetation heat flux predictions using a simple two-source model with radiometric temperatures for partial canopy cover. Agric For Meteorol 94, 13–29. https://doi.org/10.1016/S0168-1923(99)00005-2.

Li, F., Kustas, W.P., Prueger, J.H., Neale, C.M.U., Jackson, T.J., 2005. Utility of remote sensing-based two-source energy balance model under low- and high-vegetation cover conditions. J Hydrometeorol 6, 878–891. https://doi.org/10.1175/JHM464.1.

Ma, S., Baldocchi, D., Wolf, S., Verfaillie, J., 2016. Slow ecosystem responses conditionally regulate annual carbon balance over 15 years in Californian oak-grass savanna. Agric For Meteorol 228–229, 252–264. https://doi.org/10.1016/j.agrformet.2016.07.016.

Ma, S., Baldocchi, D.D., Xu, L., Hehn, T., 2007. Inter-annual variability in carbon dioxide exchange of an oak/grass savanna and open grassland in California. Agric For Meteorol 147 (3), 157–171. https://doi.org/10.1016/j.agrformet.2007.07.008.

Maseyk, K.S., Lin, T., Rotenberg, E., Grnzweig, J.M., Schwartz, A., Yakir, D., 2008. Physiology-phenology interactions in a productive semi-arid pine forest. New Phytol 178 (3), 603–616. https://doi.org/10.1111/j.1469-8137.2008.02391.x.

Meerdink, S.K., Hook, S.J., Roberts, D.A., Abbott, E.A., 2019. The ECOSTRESS spectral library version 1.0. Remote Sens Environ 230 (111196), 1–8. https://doi.org/10.1016/j.rse.2019.05.015.

Meyers, T.P., Hollinger, S.E., 2004. An assessment of storage terms in the surface energy balance of maize and soybean. Agric For Meteorol 125 (1–2), 105–115. https://doi.org/10.1016/j.agrformet.2004.03.001.

Michaletz, S., 2018. Evaluating the kinetic basis of plant growth from organs to ecosystems. New Phytol 219 (1), 37–44. https://doi.org/10.1111/nph.15015.

Miller, G.R., Chen, X., Rubin, Y., Ma, S., Baldocchi, D.D., 2010. Groundwater uptake by woody vegetation in a semiarid oak savanna. Water Resour Res 46, W10503. https://doi.org/10.1029/2009WR008902.

Nieto, H., Guzinski, R., Kustas, W. P., Andreu, A., 2020. Pytseb. https://github.com/hectornieto/pyTSEB. Date accessed: May 2020.

Nieto, H., Kustas, W.P., Torres-Rua, A., Alfieri, J., Gao, F., Anderson, M., White, W.A., Song, L., del Mar Alsina, M., Prueger, J., McKee, M., Elarab, M., McKee, L., 2019. Evaluation of TSEB turbulent fluxes using different methods for the retrieval of soil and canopy component temperatures from UAV thermal and multispectral imagery. Irrig Sci 37 (3), 389–406. https://doi.org/10.1007/s00271-018-0585-9.

Norman, J.M., Kustas, W.P., Humes, K.S., 1995. A two-source approach for estimating soil and vegetation fluxes from observations of directional radiometric surface temperature. Agric For Meteorol 77 (3–4), 263–293. https://doi.org/10.1016/0168-1923(95)02265-Y.

Pau, S., Detto, M., Kim, Y., Still, C.J., 2018. Tropical forest temperature thresholds for gross primary productivity. Ecosphere 9 (7), e023111. https://doi.org/10.1002/ecs2.2311.

Python Core Team, 2020. Python: A dynamic, open source programming language. Python Software Foundation. https://www.python.org/.

Rotenberg, E., Yakir, D., 2010. Contribution of semi-arid forests to the climate system. Science 327, 451–455. https://doi.org/10.1126/science.1179998.

Rubio, E., Caselles, V., Badenas, C., 1997. Emissivity measurements of several soils and vegetation types in the 8–14 μm wave band: analysis of two field methods. Remote Sens Environ 59 (3), 490–521. https://doi.org/10.1016/S0034-4257(96)00123-X.

Rubio, E., Caselles, V., Coll, C., Valour, E., Sospedra, F., 2003. Thermal-infrared emissivities of natural surfaces: improvements on the experimental set-up and new measurements. Int J Remote Sens 24 (24), 5379–5390. https://doi.org/10.1080/0143116031000102412.

Ryu, Y., Verfaillie, J., Macfarlane, C., Kobayashi, H., Sonnentag, O., Vargas, R., Ma, S., Baldocchi, D.D., 2012. Continuous observation of tree leaf area index at ecosystem scale using upward-pointing digital cameras. Remote Sens Environ 126, 116–125. https://doi.org/10.1016/j.rse.2012.08.027.

Song, L., Bian, Z., Kustas, W.P., Liu, S., Xiao, Q., Nieto, H., Xu, Z., Yang, Y., Xu, T., Han, X., 2020. Estimation of surface heat fluxes using multi-angular observations of radiative surface temperature. Remote Sens Environ 239, 111674. https://doi.org/10.1016/j.rse.2020.111674.

Song, L., Liu, S., Kustas, W.P., Zhou, J., Xu, Z., Xia, T., Li, M., 2016. Application of remote sensing-based two-source energy balance model for mapping field surface fluxes with composite and component surface temperatures. Agric For Meteorol 230–231, 8–19. https://doi.org/10.1016/j.agrformet.2016.01.005.

Still, C., Powell, R., Aubrecht, D., Kim, Y., Helliker, B., Roberts, D., Richardson, A., Goulden, M., 2019. Thermal imaging in plant and ecosystem ecology: applications and challenges. Ecosphere 10 (6), e02768. https://doi.org/10.1002/ecs2.2768.

Way, D., Yamori, W., 2014. Thermal acclimation of photosynthesis: on the importance of adjusting our definitions and accounting for thermal acclimation of respiration. Photosyn Res 119, 89–100. https://doi.org/10.1007/s11120-013-9873-7.

Xu, L., Baldocchi, D.D., 2004. Seasonal variation in carbon dioxide exchange over a mediterranean annual grassland in California. Agric For Meteorol 123 (1), 79–96. https://doi.org/10.1016/j.agrformet.2003.10.004.